



Klinikum rechts der Isar
Technische Universität München

M.Sc in Biomedical Engineering and Medical Physics
Technical University of Munich

Robust Single Point Ultra Short Echo Time Water Fast Separation

Mateo Rodrigo Argudo Arrieta

Supervised by:

Prof. Dr. Dimitrios Karampinos

Anh Van Tu, PhD

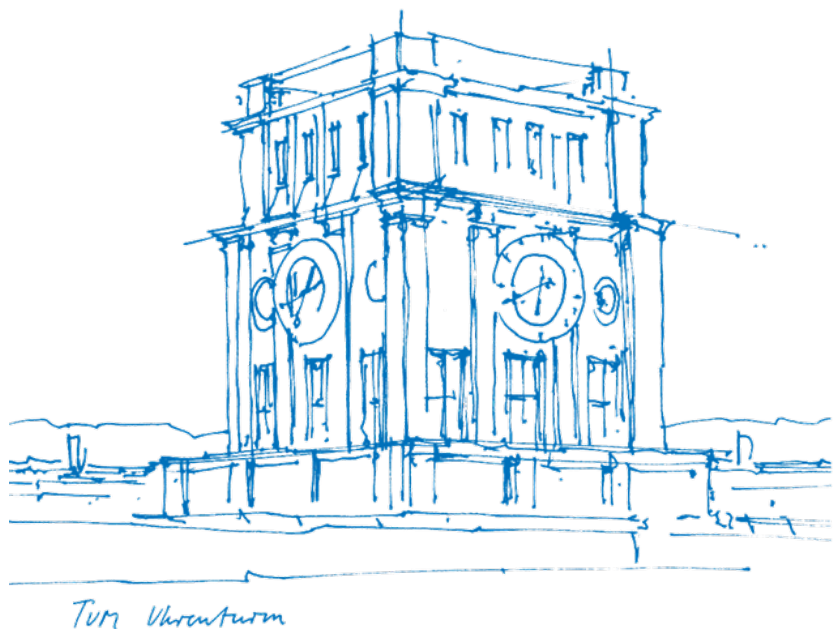
Submitted by:

Mateo Argudo

ge57des

Submitted on:

June 6, 2024



TUM Uhrenturm

DECLARATION

I hereby declare that the thesis submitted is my own unaided work. All direct or indirect sources used are acknowledged as references.

I am aware that the thesis in digital form can be examined for the use of unauthorized aid and to determine whether the thesis as a whole or parts incorporated in it may be deemed as plagiarism. For the comparison of my work with existing sources, I agree that it shall be entered into a database where it shall also remain after examination, to enable comparison with future theses submitted. Further rights of reproduction and usage, however, are not granted here.

This thesis was not previously presented to another examination board nor published.

Name: Mateo Rodrigo Argudo Arrieta

Date: June 6, 2024

Place: Munich

ABSTRACT

Water–fat (WF) MRI or Dixon imaging is a set of techniques used in the assessment of metabolic dysfunction-related diseases. These techniques leverage the frequency shift between water and fat MR signals to separate them into two images, needing the acquisition of images at multiple echo times which extends the already prolonged MRI scan duration.

Ultra short echo time (UTE) enables the visualization of short T_2^* components. When combined with Dixon imaging, UTE-Dixon provides both soft tissue and osseous contrasts that are not contaminated by the fat signal. However, the need of multiple echo times to separate water and fat prolongs the scan time. A solution is to separate water and fat with the use of a single echo time instead of multiple, shortening scan time. This technique is called single-point UTE (sUTE) Dixon imaging. The use of a single echo to separate water and fat introduces complexity to the problem, since some background phase contributions, coming from B_0 and B_1 field inhomogeneities cannot be implicitly deduced from only one echo. Hence, the problem becomes ill posed.

New techniques have arisen to tackle this ill-posed problem such as Kronthaler [21] with the use of a second order iterative optimization method (Gauss-Newton Method) with a smoothness constraint. Because the problem is ill posed initialization is necessary to ensure a proper convergence path and a better result of the water-fat separation.

This study aims to explore different methods to improve sUTE-Dixon imaging by addressing two different points:

1. Characteristics of background phase contributions and how to model them.
2. How initialization techniques changes the behavior of the iterative optimization method results.

To achieve this aims, we developed a sUTE-Dixon reconstruction framework based on the work of Kronthaler et. al. and integrated initialization techniques to further improve the method. This framework is used to compare reconstruc-

tions of different phantoms and anatomies with different hyper-parameters and initialization approaches.

Our findings reveal that the initialization, not only prevents artifacts in reconstructed images but also significantly enhances the achievable water-fat separation quality. However, there are two principal limitations of the current framework:

1. Its inability to accurately reconstruct water and fat at the anatomy/object edges.
2. Its sensitivity to mean phase shifts from the scan.

*My mother made me a scientist without ever intending to.
Every other mother in Brooklyn would ask her child after school,
So? Did you learn anything today? But not my mother.
Izzy, she would say, did you ask a good question today?
That difference - asking good questions - made me become a scientist.*

— Isidor Isaac Rabi: creator of the MRI

ACKNOWLEDGMENTS

A special thanks to Dimitrios C. Karampinos for supervising my thesis and being my guide in many decision I took throughout the thesis. For the clever suggestions and thoughtful insights, and for helping me learn about the MR scans in practice.

To Anh Tu Van as my scientific supervisor, always being supportive and attentive to any questions I had, and for helping me overcome difficult questions during the project. Also for being understanding and standing up for me in the ISMRM conference I could not attend. Thank you also for assisting me in the phantom and lung scans.

To Kilian Weiss for helping me in the MR scans, and also intelligent advice during the regular meetings of the project.

To Christian Boehm for providing me guidance with the BMRR python library and its utilities.

To Jonathan Stelter for supporting me with the server setup and questions during the project.

To my family Victor, Veronica, Miguel and Bebo, for being always, supporting me in this very important step of my formation.

To Daniela Bolaños, for backing me up in difficult times and encourage me to work harder.

And to the whole BMRR team for assisting me in this beautiful journey and being a friendly and supportive workspace during the thesis.



CONTENTS

1	Thesis Introduction	2
2	MRI Theory	7
2.1	Nuclear Magnetic Resonance (NMR)	7
2.1.1	Nuclear Spin and Magnetic Moment	7
2.1.2	Zeeman Effect	8
2.1.3	Bulk Magnetization	10
2.1.4	Resonance and radio-frequency Excitation	10
2.1.5	Relaxation Mechanisms	12
2.2	Magnetic Resonance Imaging (MRI)	14
2.2.1	Hardware Components of an MR scanner	14
2.2.2	Spatial Encoding and k-space sampling	15
2.2.3	k-Space and Image Reconstruction	18
2.2.4	Imaging Sequences	18
2.2.5	Image reconstruction	21
3	Water Fat MRI	24
3.1	Chemical Shift Encoding (CSE)	24
3.2	Multi-TE Dixon Imaging	26
3.3	Single-TE Dixon Imaging	27
4	Ultra Short Echo Time Imaging (UTE)	30
4.1	Imaging Short T_2 tissues	30
5	Single ultra short echo time Dixon imaging (sUTE-Dixon)	33
5.1	The study	33
5.1.1	The iterative optimization method	34
5.1.2	Limitations and Motivation	35
6	Thesis focus: Towards a robust single ultra short echo time Dixon imaging	38
6.1	Background Phase Contributions	38
6.1.1	Experiments	39
6.1.2	B_0 effect	40
6.1.3	B_1 effect	42
6.1.4	Quantitative Comparison	46
6.2	Initialization of the iterative optimization method in clinical applications	48

6.2.1	The Algorithm	48
6.2.2	Impact on ϕ^*	51
6.2.3	Impact on Water-Fat Separation	52
6.3	B_0 modeling as a pre-initialization	57
6.3.1	Validation	57
6.3.2	Water-Fat Separation in the Lung	58
7	Discussion	63
7.1	Phase contributions	63
7.2	Initialization Impact on Water-Fat Separation	64
7.2.1	Impact on ϕ^*	64
7.2.2	Effects on Water-Fat separation	64
7.3	Impact of B_0 modeling	66
7.3.1	Validation	66
7.3.2	Impact on Lung scans	66
7.4	Limitations	67
7.5	Implications	68
8	Conclusion	69
	Bibliography	71
A	Appendix	77
A.1	Testing different modeling functions for B_1	77
A.2	Additional clinical anatomies	82

LIST OF FIGURES

- Figure 2.1 Zeeman effect on an energy level for a nucleus with nuclear spin $I = 1/2$. The energy difference between the levels is half the Larmor frequency ω_L multiplied by \hbar . [9](#)
- Figure 2.2 Effective magnetic field and *flipping* in the rotating frame of reference. (a) The effective field \vec{B}_{eff} is a superposition of the static magnetic field \vec{B}_0 and the oscillating RF field \vec{B}_1 . (b) In case of resonance $\omega_{RF} = \omega_L$: The magnetization is deflected by the flip angle α around the x' -axis during the RF pulse, then precession occurs around the z-axis till equilibrium is achieved again. [12](#)
- Figure 2.3 Diagram illustrating the transverse (T_2 and T_2^*) relaxation processes following a 90° RF pulse. Initially, the transverse magnetization (red arrow) is at its maximum amplitude with proton magnetic moments (spins) in phase. Over time, these spins move out of phase, leading to a decay in the amplitude of the transverse magnetization and the detected signal, known as Free Induction Decay (FID). The T_2^* relaxation process encompasses both T_2 relaxation and additional dephasing effects due to field inhomogeneities. The effective decay is represented by the T_2^* time constant, which is faster than the T_2 time constant. The signal decays to 37% of its initial value within one T_2 or T_2^* time constant, respectively. Figure taken from [30] [14](#)

- Figure 2.4 The selective excitation technique is depicted above. Because we want to excite only specific frequencies in a specific band width Δf , the selective excitation pulse is a time-modulated RF pulse must be described by the Fourier homologous of the box-car function, the sinc function, as in [Equation 2.26](#). Figure adapted from [2] [16](#)
- Figure 2.5 The different encoding methods are depicted above. The phase accumulation or decrement is ruled by [Equation 2.27](#) differentiating in the x direction. Whereas the x direction is governed by the frequency encoding, with its signal given by [Equation 2.28](#). Figure adapted from [5] [17](#)
- Figure 2.6 Spin echo sequence, and spin echo formation. A 90° ($\frac{\pi}{2}$) pulse excites the spins into the transverse plane. Following, the spins dephase and accumulate phase over a period of time $\tau = \frac{TE}{2}$. Then, a 180° (π) pulse inverts the accumulated phases. Finally, the spins rephase and form an echo at $t = 2\tau = TE$. Figure adapted from [35] [20](#)
- Figure 2.7 Gradient echo sequence. A 90° ($\frac{\pi}{2}$) pulse excites the spins into the transverse plane, and the slice selection gradient is also applied. The phase encoding is done as normal and the gradients in the frequency encoding direction are chosen such that at time TE we capture an echo signal. Figure from [29] [21](#)
- Figure 3.1 Fat spectrum of an MR scan. The spectra were shifted and displayed such that the main fat peak is at 420 Hz relative to water. The spectrum depicts a multi-peak pattern. Six peaks can be identified, and their chemical shift frequencies relative to the water resonance frequency at 3T are labeled. Image adapted from [37] [25](#)
- Figure 4.1 UTE Imaging Sequences. [31](#)
- Figure 6.1 The phantom. Three parts of water to one part of oil was mixed. To avoid velocity effects it was let to rest for a couple of minutes before scanning. A thoracic coil is used to enhance the signal [39](#)

- Figure 6.2 a) UTE unwrapped phase for phantom without added salt. A smooth plain phase can be seen from the image in the water and fat regions. b) Phase for phantom with added salt. A polynomial variation of the phase can be seen from the image in the water region due to higher conductivity because of the salt. The inner part of the object has a greater effect than the outer part. [40](#)
- Figure 6.3 B_0 phases for the phantom. a) The B_0 modeled phase done via [Equation 6.3](#). b) Measured B_0 . The values of the B_0 phase are small in comparison with the UTE phase ranging from (-0.5, 0.5) rad. [41](#)
- Figure 6.4 1. Reference UTE phase, 2. B_0 filtered UTE phases for the phantom with a) and without b) added salt. The B_0 modeled phase was subtracted from the phase. a) & b): There is no noticeable difference between the reference phases (1.) and the images here. This lightly supports the assumption that B_0 field inhomogeneities is not the driving background phase phenomenon. [42](#)
- Figure 6.5 a) UTE unwrapped phase for the phantom with added salt. b) Surface plot of the UTE phantom slice. The phase of the phantom in the water species resembles an even 3D polynomial. Which supports the approach of using a second-degree 3D polynomial fit for modeling the B_1 phase. [43](#)
- Figure 6.6 a) Modeled [rad] and b) ground truth [% $\Delta\alpha$] B_1 maps of the phantom without salt.(1.) and the phantom with added salt (2.). **NOTE:** Its quantitative comparison is difficult since the DREAM method returns the percentage of change relative to the main flip angle, whereas the phase is modeled directly from the polynomial fit, and its conversion is not possible. [44](#)

- Figure 6.7 1. Reference UTE phase, 2. B_1 filtered UTE phases. a) Phantom without salt. b) Phantom with salt. The images are smoother than the reference UTE phases (1.), specially in the phantom with added salt a great improvement is seen, but not without its imperfections, such as some artifacts at the phantom edges. 45
- Figure 6.8 Water Fat separation. a) Water b) Fat. The separation is correct and much smoother in the phantom without added salt, as expected, because of the UTE-phase shape as depicted in the contour plot in Figure 6.5. 45
- Figure 6.9 Zoomed line-plots through water (1.) & fat (2.). It is shown how the curvature of the raw UTE phase cannot be correctly approximated by the forward modeled phase of B_0 . On the other hand the B_1 modeled phase with the 2nd degree 3D polynomial has no problem adapting to the slight curvature of the phase inside the phantom. 46
- Figure 6.10 Gauss Newton Optimization with Initialization. The algorithm is divided in three main parts. 1. The signal UTE phase is unwrapped and taken as input of the polynomial fit. The output of this fit is the first guess of the background phase ϕ_{init} . 2. This background phase gets filtered out from the raw signal obtaining a filtered phase $S_{filtered}$ and from this the first guesses of the water and fat are calculated W_{init}, F_{init} . 3. The guesses $\phi_{init}, W_{init}, F_{init}$ are then input as initialization of the Gauss Newton optimization algorithm, from which we get the final water-fat separation with the final fitted background phase W, F, ϕ . 50

- Figure 6.11 Resulting ϕ^* from the Gauss Newton (GN) and Gauss Newton with Initialization (GN with Init.) methods for the regularization parameters $\lambda = 1, 10, 100$. With increasing regularization the resulting phase is enforced to be smoother, approaching to the plain polynomial fit solution. The number of iterations till convergence are shown above every image. The initialized algorithm provides a good initialization, reducing the number of iterations substantially for every regularization parameter. 52
- Figure 6.12 Resulting Water and Fat of the cervical spine from the Gauss Newton and Gauss Newton with Initialization methods for the regularization parameters $\lambda = 1, 10, 100$. The overall water-fat separation from the initialized algorithm delivers a better quality than the plain algorithm. Specially at the brain and bone. 53
- Figure 6.13 Resulting Water and Fat from the Gauss Newton (GN) and Gauss Newton with Initialization (GN with Init.) methods for regularization $\lambda = 100$. The water-fat separation of the brain and bone is superior in the initialized method. Although some artifacts at the edges are still seen (green arrows), also some artifacts are dimmed (red arrows), proving an overall better water-fat separation. 53
- Figure 6.14 Resulting Water and Fat for the thoracic spine from the Gauss Newton and Gauss Newton with Initialization methods for the regularization parameters $\lambda = 1, 10, 100$. The water-fat separation is qualitatively the same for both cases. No stability is lost with increasing regularization. 54
- Figure 6.15 Resulting fat from the Gauss Newton (GN) and Gauss Newton with Initialization (GN with Init.) methods for regularization $\lambda = 100$. Separation delivers roughly the same quality on both methods. Although the separation of the skin fat is improved by the initialization(green arrows), and some streaking artifacts in the inner abdomen are dimmed (red arrows). 55

- Figure 6.16 Resulting Water and Fat for the lumbar spine from the Gauss Newton and Gauss Newton with Initialization methods for the regularization parameters $\lambda = 1, 10, 100$. The water-fat separation is qualitatively the same for small regularization. But stability is rapidly lost with increasing regularization for the non-initialized method, while its counterpart remains robust. [55](#)
- Figure 6.17 Resulting fat from the Gauss Newton (GN) and Gauss Newton with Initialization (GN with Init.) methods for regularization $\lambda = 100$. There is a substantial difference between the water fat separation of the non-initialized versus the initialized method. The initialized method delivers a fairly correct water-fat separation. Whereas the non-initialized method stops delivering a good separation quality for regularization $\lambda = 100$ [56](#)
- Figure 6.18 Resulting Water and Fat of the cervical spine from the forward modeled and plain initialized Gauss Newton methods for the regularization parameters $\lambda = 1, 10, 100$. The results have virtually the same quality. [58](#)
- Figure 6.19 Resulting Water and Fat of the thoracic spine from the forward modeled and plain initialized Gauss Newton methods for the regularization parameters $\lambda = 1, 10, 100$. The results have virtually the same quality. [58](#)
- Figure 6.20 Resulting Water and Fat of the lumbar spine from the forward modeled and plain initialized Gauss Newton methods for the regularization parameters $\lambda = 1, 10, 100$. The results have virtually the same quality. [60](#)
- Figure 6.21 Resulting B_0 induced phase map for a lung scan. The used lung mask is implicitly seen from the different phase inside the lungs. [60](#)

- Figure 6.22 Resulting Water and Fat of the lung from the forward/no-forward modeled methods for the regularization parameters $\lambda = 1, 10, 100$. The results for the forward/no forward modeling are similar for medium-high regularization. But for low regularization $\lambda = 1$ the separation is better without the B_0 pre-initialization. 60
- Figure 6.23 Resulting Water and Fat of the lung from the forward/no-forward modeled methods for the regularization parameters $\lambda = 1, 10, 100$. The results for the forward/no forward modeling are only similar for high regularization. But for low and medium regularization $\lambda = 1, 10$ the separation is better without the B_0 pre-initialization. 61
- Figure A.1 Water-Fat separation comparison of the fitting functions 2^{nd} versus 4^{th} degree 3D polynomial for initialization. From top to bottom the cervical spine, thoracic spine and lumbar spine results are depicted. The red boxes indicate the important points for the comparison of both images. The second degree polynomial seems the superior choice between the two. 78
- Figure A.2 Water-Fat separation and line-plot comparison of the fitting functions 2^{nd} versus 4^{th} degree 3D polynomial for initialization. It is illustrated how the 4^{th} degree polynomial over-fits the image slightly, whereas, the 2^{nd} degree polynomial acts an implicit regularizer because of its coarseness. 79
- Figure A.3 Water-Fat separation comparison of the fitting functions 2^{nd} degree 3D polynomial versus using the UTE phase for initialization. From top to bottom the cervical spine, thoracic spine and lumbar spine results are depicted. The red and blue boxes indicate the important points for the comparison of both images. The second degree polynomial seems the superior choice between the two. Although in the cervical spine the UTE phase initialization reduces the anatomy edges artifacts. 81

- Figure A.4 Water-Fat separation of the Knee for the plain Gauss Newton and the initialized method. There is no visible difference between both methods. [82](#)
- Figure A.5 Water-Fat separation of the Lung for the plain Gauss Newton and the initialized method. There is improvement of the water-fat separation at low regularization, since the heart has more content of water in the initialized method. For high regularization, the initialized method depicts the separation better and its more stable. Mid regularization results show no discernible difference. [83](#)
- Figure A.6 Water-Fat separation of the liver for the plain Gauss Newton and the initialized method. The initialized method partially reassigns the liver region to water across all λ values, resulting in a separation that, while not entirely accurate, is substantially more correct than that achieved by the non-initialized method. [83](#)

LIST OF TABLES

- Table 6.1 Flatness measurements for different regions of the phantoms filtered phase. The phase is filtered by subtracting the modeled B_0 and B_1 effects on the background phase of the signal. Note that the sum of gradients is done in species regions lightly smaller than the real area to avoid high spikes at borders. That is why the sum of gradient over the whole image is different than the sum of both water and fat sum of gradients separately. [47](#)
- Table 6.2 Measurement Parameters. For all the scans a sagittal orientation, a flip angle of 5° , and a SENSE factor of $R = 1.5$ was used. [51](#)

ACRONYMS

MRI Magnetic Resonance Imaging

CT Computed Tomography

NMR Nuclear Magnetic Resonance

MR Magnetic Resonance

wF Water-Fat

PDFF Proton Density Fat Fraction

cse Chemical Shift Encoding

UTE Ultra-Short Echo Time

RF Radio Frequency

FID Free Induction Decay

TE Echo Time

TR Repetition Time

IP In-Phase

OP Out-of-Phase

FOV Field of View

GRE Gradient Echo

SE Spin Echo

DREAM Dubbed Dual Refocusing Echo Acquisiton Mode

L-BFGS Limited-Memory Broyden–Fletcher–Goldfarb–Shanno Algorithm

GN Gauss–Newton

INTRODUCTION TO WATER FAT SEPARATION IN MRI

THESIS INTRODUCTION

Magnetic Resonance Imaging (MRI) is a fundamental tool in radiology and biomedical research, offering capabilities for both anatomical and functional imaging. MRI excels in providing superior soft-tissue contrast compared to CT scans and delivers higher resolution images than ultrasound, all while being a generally safe method with infrequent occurrences of patient harm [25] and no exposure to ionizing radiation.

MRI operates based on the Nuclear Magnetic Resonance (NMR) phenomenon to create changes in magnetization that are detectable by its receiver systems. It achieves spatial localization by stimulating nuclear spins within an external magnetic field. By modifying the imaging sequences, MRI can manipulate spin systems to produce various contrasts, such as relaxation, proton density, diffusion, and phase contrasts. Beyond producing diagnostic-quality images, MRI can also be adapted for quantitative analysis, which has spurred developments in creating maps of tissue physical properties for quantitative clinical interpretations.[12]

Globally, over 25,000 MRI scanners are in use, supporting a wide range of diagnostic and therapeutic applications. In neuroimaging, MRI is crucial for distinguishing between gray and white matter, aiding in the diagnosis of conditions like dementia, Alzheimer's disease, demyelinating diseases, epilepsy, and anomalies in the brain and spinal cord. It also facilitates diffusion and functional imaging techniques that can map neuronal tracts and blood flow. Cardiovascular uses of MRI include examining the structure and function of the heart and assessing vascular diseases. In musculoskeletal imaging, MRI is used for evaluating joints, spine, soft tissue tumors, and muscle disorders. Additionally, MRI is employed in abdominal assessments for the liver, gastrointestinal tract, breasts, and prostate, particularly useful in detecting cysts, tumors, and other abnormalities. Functional imaging of metabolites through spectroscopy is also a capability of MRI. [1]

In diagnostic imaging, fat presents a crucial MR signal component that often needs to be suppressed or differentiated from water signals. This manipulation is vital for accurate quantification of MR properties in tissues characterized by mixed chemical shifts. Particularly, imaging of short- T_2 tissues requires significant suppression of long- T_2 signals from both water and fat to enhance image contrast and clarity. The technology of water-fat (WF) imaging has evolved into state-of-the-art imaging methodology essential for differentiating between water and fat signals. These methods are particularly useful for qualitative purposes, such as suppressing the fat signal, or they are used quantitatively to derive bio-markers of tissue fat concentration such as the Proton Density Fat Fraction (PDFF). Furthermore, water-fat MRI is particularly useful for assessing diseases linked to metabolic disorders, such as obesity, metabolic syndrome, and type-2 diabetes [3, 9]. The ability to effectively manage fat signals in MRI is useful for improving the diagnostic accuracy of MRI scans and they not only provide a clearer visualization of anatomical structures but also facilitate a better understanding of tissue compositions, which is crucial for accurate diagnosis and treatment planning. [22]

This method utilizes chemical shift encoding (CSE) techniques, also known as Dixon imaging, capitalizing on the chemical shift differences between water and fat MR signals to differentiate them and create the two respective distinct images. The water-fat separation process involves fitting the acquired signal to a physical model, typically necessitating multiple image captures at different echo times. This requirement extends the scan duration, and coupled with the inherently slow MRI acquisition speed, increases the susceptibility of the technique to motion artifacts from patient or physiological movement. Techniques such as respiratory triggering or breath-hold are employed to minimize these artifacts, though they may elevate patient discomfort. Therefore, there is a pressing need to develop methods to expedite the MRI scanning process.

The challenge of imaging short T_2^* tissues in MRI is well-recognized, with a significant body of research focused on UTE Dixon imaging techniques, which are used to both suppress fat signal in UTE acquisitions and to determine tissue electron density properties. Where its most important applications are on the determination of the attenuation correction in positron emission tomography (PET), and on the imaging of short T_2^* tissues in musculoskeletal radiology. [22].

Specifically single-echo/single-point UTE Dixon techniques have been developed for fast acquisition with promising water-fat separation results. Because

of the short echo times the R_2^* relaxation is negligible making it easier to image short T_2^* tissues, but it amplifies the relative effects of B_0 & B_1 field inhomogeneities affecting the quality of the water-fat separation since the signal is not strong. Moreover, by using only one complex image some background phase effects cannot be mapped in a straight forward manner, such as with B_0 & B_1 mapping, translating into a more complex problem that requires background phase corrections for a reliable WF separation.

In this context, multiple sUTE-Dixon methods have been developed for imaging tissues with short T_2^* for fat suppression, long- T_2 signal suppression and water-fat imaging [17, 21]. Jang et al. [17] corrected this phase effects via an additional field map extracted from a dual-echo UTE acquisition. Then a single-point Dixon method is used on a non-UTE signal to obtain the fat map and suppress it in the UTE image. This method proved to have a higher contrast to noise ratio (CNR) for short T_2 tissues than conventional fat suppression methods. However, this requires additional acquisitions. Also, if there are strong B_0 field inhomogeneities that the shimming cannot correct the background phase ϕ_{bulk} can become so large that the reference scan may reproduce significant errors.

Kronthaler S., et. al [21] developed a method that, in contrast to Jang et al. avoids calibration measurements. The technique uses an iterative optimization method to solve the water-fat separation problem, trying to capture the background phase to remove it from the signal and continue with the classic separation algorithm. The method reproduced high quality water-fat separated images. But, although the algorithm tries to regularize the image by rewarding smoothness of the fitted phase, the problem is still ill posed and without proper initialization the stability of the algorithm may not deliver its full potential.

The purpose of this study is to analyze different modeling approaches of background phase contributions and various initialization techniques for the algorithm in Kronthaler S., et. al [21]; comparing it qualitatively with the original algorithm and studying its effects on the resulting water-fat separation quality and stability of the algorithm.

Thesis Structure

The thesis is organized into the following chapters:

- **Chapter 1:** The current chapter presents a brief introduction, motivation and purpose of the thesis.

- **Chapter 2:** Resumes the general theory of MRI, including signal generation, signal encoding, k-space and echo sequences.
- **Chapter 3:** Introduces the UTE sequences and the water fat separation of MRI signals.
- **Chapter 4:** Analyses the different background phase contributions and its effects in the resulting MRI acquisition.
- **Chapter 5:** Introduces the iterative optimization method used for water-fat separation and analyses the impact of different initialization strategies on its resulting water and fat images.
- **Chapter 6:** Summarizes the conclusions drawn from various results from the previous chapters.

THEORY OF MAGNETIC RESONANCE IMAGING

In this chapter we will introduce the theory of magnetic resonance imaging. We will start with the physics background in nuclear magnetic resonance, following to signal acquisition in k-space and signal encoding. Finally, echo sequences are introduced.

2

MRI THEORY

2.1 NUCLEAR MAGNETIC RESONANCE (NMR)

Nuclear Magnetic Resonance (NMR) is the physical phenomenon underlying magnetic resonance imaging (MRI). NMR occurs when nuclei with non-zero spin absorb and emit electromagnetic radiation when the nuclei are placed in an external magnetic field. Most isotopes with an odd number of protons and/or neutrons such as hydrogen (^1H), carbon (^{13}C), and phosphorus (^{31}P) have a spin [26].

^1H is the most abundant isotope inside the body and is the commonly used nuclei in magnetic resonance imaging. Its properties such as a high gyro-magnetic ratio, and a non-zero spin, makes it suitable for conducting measurements that provides information about the structure of the scanned tissue. For interested readers we refer to the standard literature [13, 23]

2.1.1 Nuclear Spin and Magnetic Moment

Nuclei with an odd number of protons and/or neutrons possess a property called nuclear spin $\tilde{\mathbf{I}}$ of a nucleus with mass A . Since nuclei are not single entities, $\tilde{\mathbf{I}}$ is composed of the spins \vec{s}_i and the orbital angular momenta \vec{l}_i of the protons and neutrons in the nucleus which have a spin $s = \frac{1}{2}$. Its relation is described by:

$$\tilde{\mathbf{I}} = \sum_{i=1}^A (\vec{s}_i + \vec{l}_i). \quad (2.1)$$

Different nuclear spin configurations can be achieved depending on the number of protons and neutrons in the nucleus, with the quantum relations given by:

$$\hat{\tilde{\mathbf{I}}} |I, m\rangle = \hbar^2 I(I+1) |I, m\rangle \quad (2.2)$$

$$\hat{I}_z |I, m\rangle = \hbar m |I, m\rangle \quad (2.3)$$

with $\|\vec{I}\| > 0$, using the spin operator $\hat{\vec{I}}$, m as the magnetic quantum number, and constant $\hbar = \frac{h}{2\pi}$ is the reduced Plank's constant $6.6 \times 10^{-34} \text{ J s}$ divided by 2π .

The nuclear spin can be related to a microscopic magnetic field which is formed by the charged nuclei rotating around its axis. The nuclear magnetic moment $\vec{\mu}$ is directly to the total spin angular momentum \vec{I} :

$$\vec{\mu} = \gamma \vec{I}, \quad (2.4)$$

where the proportionality constant γ , known as gyro-magnetic ratio, depends on the atomic nucleus.

To get the magnitude of $\vec{\mu}$ we use:

$$\|\vec{\mu}\| = \gamma \hbar \sqrt{I(I+1)}, \quad (2.5)$$

where I is the nuclear spin quantum number with values $I = 0, \frac{1}{2}, 1, \frac{3}{2}, \dots$. With the help of [2.1](#) we can derive:

- nuclei with odd A have half-integer I , e.g.: ^1H , ^{13}C .
- nuclei with even A and charge have $I = 0$, e.g.: ^{12}C , ^{16}O .
- nuclei with even A and odd charge have integer I , e.g.: ^2H , ^6Li , ^{14}N .

Hydrogen (^1H) has a relatively high gyro-magnetic ratio and is also one of the most abundant nuclei with non-zero spin in human tissue, which makes it perfect for MRI acquisitions.

2.1.2 Zeeman Effect

This magnetic moment points at a random direction in absence of a magnetic field, thus free spin systems have a spherical distribution of spin orientations due to the Boltzmann equation for thermal energy. In the presence of a magnetic field \vec{B}_0 , $\vec{m}\vec{\mu}$ aligns in the direction of the field and we can obtain the energy:

$$\mathcal{H} = -\vec{\mu} \cdot \vec{B}_0. \quad (2.6)$$

Without loss of generality we can assume that $\vec{B}_0 = B_z \vec{e}_z$. Then, the Hamiltonian can be reformulated using [Equation 2.4](#) to:

$$\mathcal{H} = -\gamma I_z B_0. \quad (2.7)$$

Hence, the eigenstates of $\hat{\mathcal{H}}$ correspond to the eigenstates of \hat{I}_z , which in turn comprise of $2l + 1$ different values. Thus, we can denote the energy levels by:

$$E_m = -\gamma \hbar B_0 m, \quad -I \leq m \leq I, \quad (2.8)$$

which resembles an angular momentum $\vec{m}u$ precessing with the angular frequency $\gamma B_0 = \omega_L$, known as the *Larmor* frequency. [19]

The resulting splitting of a single non-excited energy level into several new excited levels in the presence of an external magnetic field is called Zeeman effect depicted in Figure 2.1. With the energy difference between energy levels:

$$\Delta E = |E_{m+1} - E_m| = \hbar \gamma B_0 = \hbar \omega_L. \quad (2.9)$$

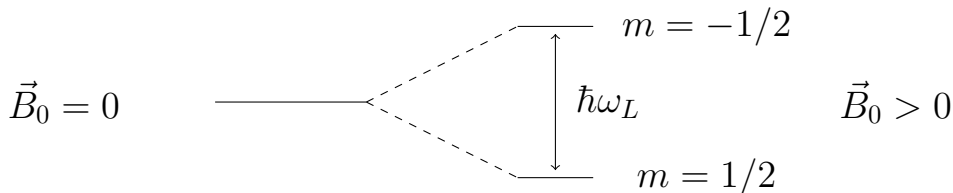


Figure 2.1: Zeeman effect on an energy level for a nucleus with nuclear spin $I = 1/2$. The energy difference between the levels is half the Larmor frequency ω_L multiplied by \hbar .

A spin system may have multiple resonant frequencies when presented with field inhomogeneities, shielding from neighboring spins, etc. This is called *chemical shift* which is described by a shielding constant δ :

$$\begin{aligned} B_0^{eff} &= B_0(1 - \delta) \\ \omega &= \omega_0 - \Delta\omega = \omega_0(1 - \delta) \end{aligned} \quad (2.10)$$

As an example, the hydrogen nuclei in a fat molecule CH_2 have a shielding constant of $\delta = 3.35$ ppm with respect to a proton in water.

The gyro-magnetic ratio of the proton (${}^1\text{H}$) is $\gamma = 1.675\ 221\ 9 \times 10^8 \text{ s}^{-1} \text{ T}^{-1}$, which corresponds to a frequency of $f = \frac{\omega_L}{2\pi} = 127.732 \text{ MHz}$ for $B_0 = 3 \text{ T}$.

2.1.3 Bulk Magnetization

The magnetic moments of N atomic nuclei sum up to a net bulk magnetization \vec{M} that describes the behavior of the system:

$$\vec{M} = \sum_{i=1}^N \vec{\mu}_i. \quad (2.11)$$

Because in absence of an external magnetic field the nuclei in the human body are at thermal equilibrium, and the thermal energy is large compared to the energy of the non-excited spin state ($k_B T \gg \gamma \hbar B_0$) the occupation density of the spin states can be expressed using Boltzmann statistics. Hence, we can derive that the excess rate of spins pointing on a specific direction vs the spins pointing at the opposite direction can be described by the Boltzmann distribution:

$$\frac{N_\uparrow}{N_\downarrow} = \exp\left(\frac{\Delta E}{k_B T}\right). \quad (2.12)$$

where k_B is the Boltzmann constant.

Since $k_B T \gg \Delta E$ we can approximate to the first order [Equation 2.12](#). Thus denoting the excess spins N_s we derive the bulk magnetization as:

$$M_z^0 = \|\vec{M}\| \approx \frac{\gamma^2 h^2 B_0 N_s}{4 k_B T}. \quad (2.13)$$

At room temperature ($T = 300$ K), the number of spins in the up-state is almost equal to the number of spins in the down-state. Nevertheless, the high abundance of hydrogen in the human body generates sufficient bulk magnetization for imaging purposes.[\[23\]](#).

2.1.4 Resonance and radio-frequency Excitation

The dynamics of the bulk magnetization can be derived similarly as with $\vec{\mu}$ [\[14\]](#):

$$\frac{d\vec{M}}{dt} = \gamma \vec{M} \times \vec{B} \quad (2.14)$$

In equilibrium [Equation 2.14](#) is equal to 0, and similar to μ the bulk magnetization is parallel to the external magnetic field \vec{B} . In this state, no signal is

produced, hence, an external time-changing magnetic field must be applied. This is achieved by applying radio-frequency (RF) excitation.

When nuclei are subjected to a radio-frequency pulse at resonance, they absorb energy and are excited to a higher energy state deflecting the bulk magnetization out of equilibrium. The resonance condition is met when the frequency of the RF pulse matches the Larmor frequency ($\omega_L = \gamma B_0$). This causes the net magnetization vector to tip away from the \vec{B}_0 axis (w.l.o.g \vec{e}_z), creating transverse magnetization. The form of such RF pulse can be described by:

$$\vec{B}_1(t) = B_1^e(t) \exp^{-i\omega_{RF} \cdot t + \phi} \quad (2.15)$$

where \vec{B}_1 is a circularly polarized magnetic field in the xy-plane with an envelope $B_1^e(t)$ the resonant condition is met when $\omega_{RF} = \omega_L$.

Thus, the external magnetic field can be depicted as the sum of the RF pulse and the static magnetic field $\text{vec } B_0$:

$$\vec{B} = \begin{pmatrix} B_1^e(t) \cos(\omega_{RF} \cdot t - \phi) \\ -B_1^e(t) \sin(\omega_{RF} \cdot t - \phi) \\ B_0 \end{pmatrix} \quad (2.16)$$

Without loss of generality we choose a rotating frame of reference rotating at the Larmor frequency and we restrict \vec{B}_1 to only the x direction in the rotating frame of reference x'. Here the bulk magnetization dynamics can be described using the effective magnet field \vec{B}_{eff} . Using [Equations 2.14 and 2.16](#) we obtain.

$$\frac{d}{dt} \vec{M}_{rot}(t) = \vec{M}_{rot}(t) \times \gamma \vec{B}_{eff} = \vec{M}_{rot}(t) \times \gamma \begin{pmatrix} B_1 \\ 0 \\ B_0 - \frac{\omega_{RF}}{\gamma} \end{pmatrix} \quad (2.17)$$

The z-component of \vec{B}_{eff} vanishes for am RF pulse resonating at the Larmor frequency. Thus, \vec{M}_{rot} is static relative to the rotation frame of reference when there is no RF pulse. The phenomenon is depicted in [Figure 2.21](#).

When the RF pulse oscillates at the Larmor frequency [Equation 2.17](#) describes a *flip* in the bulk magnetization. This flip angle α can be calculated by:

$$\alpha = \int_0^{t_p} \gamma B_1(s) ds, \quad (2.18)$$

where t_p us the pulse duration. Its effect is depicted in Figure 2.22.

The effect of this pulses can be described by rotation matrices $\mathbf{R}(\alpha)$:

$$\vec{\mathbf{M}}_+ = \mathbf{R}_x(\alpha) \vec{\mathbf{M}}_-, \quad (2.19)$$

here, $-/+$ indicates before/after the pulse and the subscript is the axis of rotation.

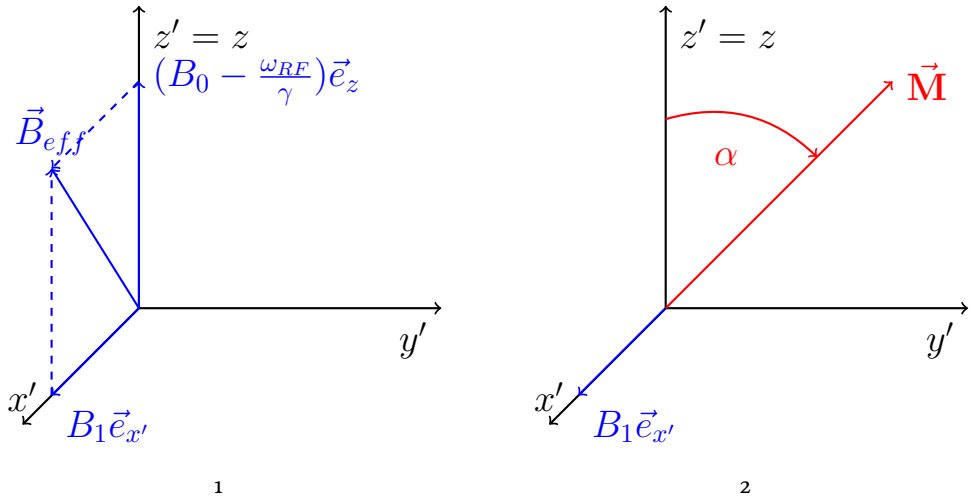


Figure 2.2: Effective magnetic field and *flipping* in the rotating frame of reference. (a) The effective field \vec{B}_{eff} is a superposition of the static magnetic field \vec{B}_0 and the oscillating RF field \vec{B}_1 . (b) In case of resonance $\omega_{RF} = \omega_L$: The magnetization is deflected by the flip angle α around the x' -axis during the RF pulse, then precession occurs around the z -axis till equilibrium is achieved again.

In MRI the sample is placed surrounded by RF coils which act as receiver and transmitters of signal. When an RF pulse is applied $\vec{\mathbf{M}}$ gets shifted from equilibrium and starts precessing to its ground state as described in Equation 2.17. This temporally varying magnetization by Faraday's law induces a current in the RF receiver coils proportional to the transverse magnetization, after amplification of the signal the measurement is done.

2.1.5 Relaxation Mechanisms

After the RF pulse is turned off, the excited nuclei return to their equilibrium state through relaxation processes. Its dynamics can be described via the Bloch equations:

$$\frac{\partial}{\partial t} \vec{\mathbf{M}}_{rot} = \vec{\mathbf{M}}_{rot}(t) \times \gamma \vec{B}_{eff} - \frac{M_{x'} \vec{e}_{x'}}{T_2} - \frac{(M_{z'} - M_z^0) \vec{e}_{z'}}{T_1}. \quad (2.20)$$

From these equations we can describe the effects that the bulk magnetization experiences after an RF pulse is applied:

- **Free Precession:** Of the bulk magnetization \vec{M} around \vec{B}_0 .
- **T₁ (Longitudinal) Relaxation:** The recovery of longitudinal magnetization M_z along the B_0 axis to the thermal equilibrium.
- **T₂ (Transverse) Relaxation:** The decay of transverse magnetization M_{xy} due to spin-spin interactions.

The signal obtained after an RF pulse is referred as Free Induction Decay (FID) signal, which refers to the transverse magnetization decay with a decay rate $R_2 = \frac{1}{T_2}$ seen in [Equation 2.20](#).

By solving [Equation 2.20](#) after the pulse ($\vec{B}_{1,+} = 0$) we can see that both relaxations behave exponentially:

$$\begin{cases} M_{x'y'}(t) = M_{x'y'}(0_+)e^{-t/T_2} \\ M_z(t) = M_z^0(1 - e^{-t/T_1}) + M_z(0_+)e^{-t/T_1} \end{cases} \quad (2.21)$$

The parameter T_1 characterizes spin-lattice relaxation, quantifying the rate at which the longitudinal component of magnetization, aligned with the static magnetic field, reverts to thermodynamic equilibrium through energy exchange with its environment.

Spin-spin relaxation is described by the time constant T_2 , which measures the relaxation of transverse magnetization to its equilibrium state due to entropy-related effects. The effective transverse relaxation time, denoted as T_2^* , incorporates the impact of static magnetic field inhomogeneities ΔB_0 :

$$\frac{1}{T_2^*} = \frac{1}{T_2} + \gamma \Delta B_0 = \frac{1}{T_2} + \frac{1}{T'_2}, \quad (2.22)$$

where T'_2 is the decay constant because of inhomogeneities. For further analysis we use the notation for the relaxation rates $R_i = \frac{1}{T_i}$. These effects are depicted in [Figure 2.3](#).

The dephasing effect of the field inhomogeneities may be countered by a tailored signal acquisition sequence which we will talk in [Section 2.2.4](#).

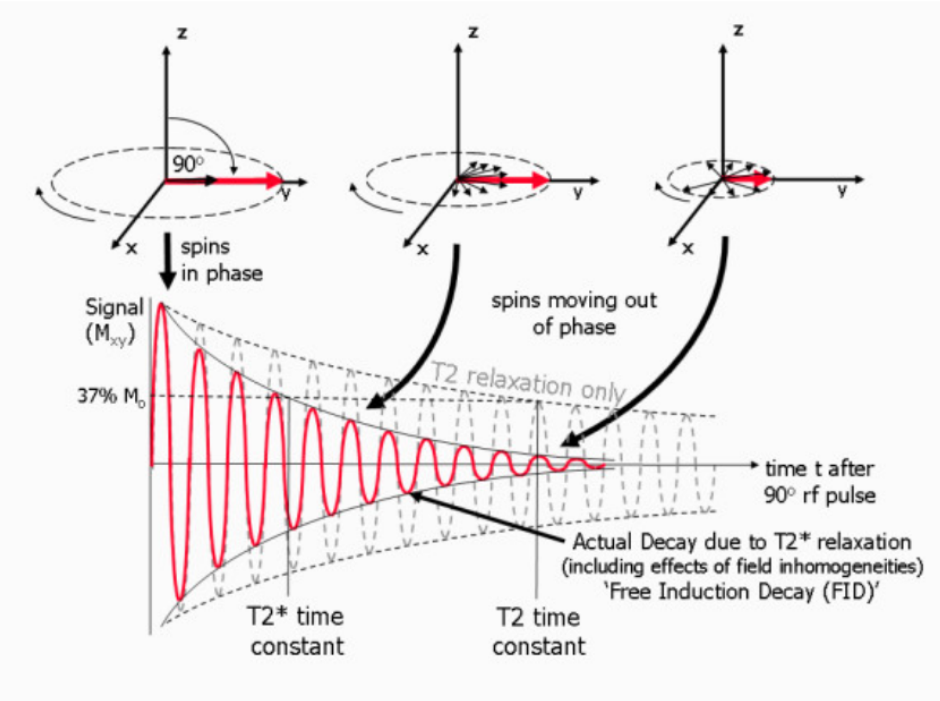


Figure 2.3: Diagram illustrating the transverse (T_2 and T_2^*) relaxation processes following a 90° RF pulse. Initially, the transverse magnetization (red arrow) is at its maximum amplitude with proton magnetic moments (spins) in phase. Over time, these spins move out of phase, leading to a decay in the amplitude of the transverse magnetization and the detected signal, known as Free Induction Decay (FID). The T_2^* relaxation process encompasses both T_2 relaxation and additional dephasing effects due to field inhomogeneities. The effective decay is represented by the T_2^* time constant, which is faster than the T_2 time constant. The signal decays to 37% of its initial value within one T_2 or T_2^* time constant, respectively. Figure taken from [30]

2.2 MAGNETIC RESONANCE IMAGING (MRI)

Nuclear magnetic resonance may be used to retrieve useful information of the body via measured signals from a series of intentional excitations which we call imaging sequences. This section studies how these signals are acquired and how an image is formed in MRI.

2.2.1 Hardware Components of an MR scanner

The main hardware components used for signal generation and acquisition of an MR scanner are:

- **Main magnet:** A permanent magnet made of superconductor material that creates an static magnetic field B_0 .
- **RF coils:** Coils that produce a *time varying* magnetic field B_1 transverse to B_0 tuned to a specific resonant frequency. They also act as receiving coils capturing the precession of the transverse magnetization by Faraday's law.
- **Gradient coils:** Coils that produce *spatially varying* magnetic fields that are used to encode the spatial information of the signal.

2.2.2 Spatial Encoding and k -space sampling

Without applying extra magnetic fields a plain resonant RF pulse generates a signal which is the sum of all its components in multiple spatial locations. Thus, for imaging complex objects there is the need of localize the generation and measurement of the signal in space. The methods used in MRI to achieve this are: selective excitation, also known as slice selection (SS), and spatial encoding.

2.2.2.1 Selective Excitation (Slice Selection)

A gradient field applied along one axis (e.g., the z -axis) selectively excites the nuclei of a slice of tissue, making the Larmor frequency position dependent:

$$f(z) = f_L + \gamma G_z z \quad (2.23)$$

The RF pulse is designed to match the Larmor frequency of the nuclei in the desired slice making the spatial selection function a boxcar-function:

$$s(z) = \prod \left(\frac{z - z_0}{\Delta z} \right) = \begin{cases} 1, & \text{if } |z - z_0| < \frac{\Delta z}{2} \\ 0, & \text{otherwise} \end{cases} \quad (2.24)$$

Or using the frequencies and Equations 2.23 and 2.24:

$$\begin{aligned} s_f(f) &= \prod \left(\frac{f - f_{z_0}}{\Delta f} \right), \\ f_{z_0} &= f_L + \gamma G_z z_0, \\ \Delta f_{BW} &= \gamma G_z \Delta z, \end{aligned} \quad (2.25)$$

where Δf_{BW} is the bandwidth of the RF pulse which indirectly defines the slice width Δz .

To obtain such RF pulse we apply the Fourier transform to the boxcar function in [Equation 2.25](#), obtaining an excitation profile of a *sinc* function:

$$B_1(t) = C \cdot \text{sinc}(\pi \Delta f \cdot t) e^{-2\pi i f_{z_0} t}, \quad (2.26)$$

C is defined by the desired flip angle. This technique is depicted in [Figure 2.4](#)

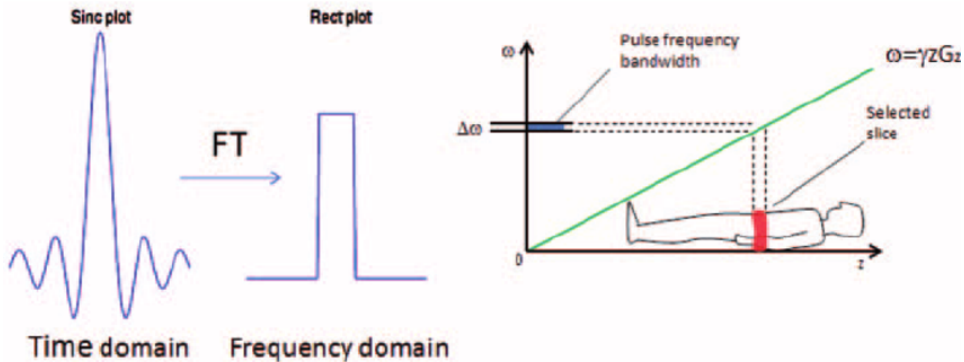


Figure 2.4: The selective excitation technique is depicted above. Because we want to excite only specific frequencies in a specific band width Δf , the selective excitation pulse is a time-modulated RF pulse must be described by the Fourier homologous of the box-car function, the sinc function, as in [Equation 2.26](#). Figure adapted from [2]

Because RF pulses cannot be infinitely long, the sinc function is truncated for a finite duration τ_p . This introduces B_1 inhomogeneities. These are reduced by suitable pulse designs such as Gaussian and hyperbolic secant pulse.

2.2.2.2 Phase and Frequency Encoding

Following slice selection a gradient is applied along a perpendicular axis (e.g., the y -axis) which introduces a position-dependent phase shift. By incrementally changing the phase-encoding gradient, spatial information along this axis is encoded. The duration of the phase encoding constant gradient \mathbf{G}_{PE} is denoted by T_{PE} . The spins, are then differentiated by the phase angle they accumulate during the pulse:

$$\phi(\mathbf{r}) = -\gamma \mathbf{G}_{PE} \cdot \mathbf{r} T_{PE} \quad (2.27)$$

A third gradient is applied along a second axis (e.g., the x -axis) causing the resonance frequency to vary linearly with position. This frequency variation is

used to encode the spatial position along this axis. Because of [Equation 2.23](#) we can encode the spatial positions by its frequency using a frequency encoding gradient \mathbf{G}_{FE} .

This information can only be retrieved during signal acquisition, that is why this type of gradients are called readout gradients. Then, the measured signal of the whole object is given by:

$$\begin{aligned} S(t) &= \int_V \rho(\mathbf{r}) e^{-i\mathbf{G}_{FE}\mathbf{r}t} d\mathbf{r} \cdot e^{-i\omega_0 t}, && \text{Gradient Echo} \\ S(t) &= \int_V \rho(\mathbf{r}) e^{-i\mathbf{G}_{FE}\mathbf{r}(t-TE)} d\mathbf{r} \cdot e^{-i\omega_0 t}, && \text{Spin Echo} \end{aligned} \quad (2.28)$$

The encoding methods are depicted in [Figure 2.5](#).

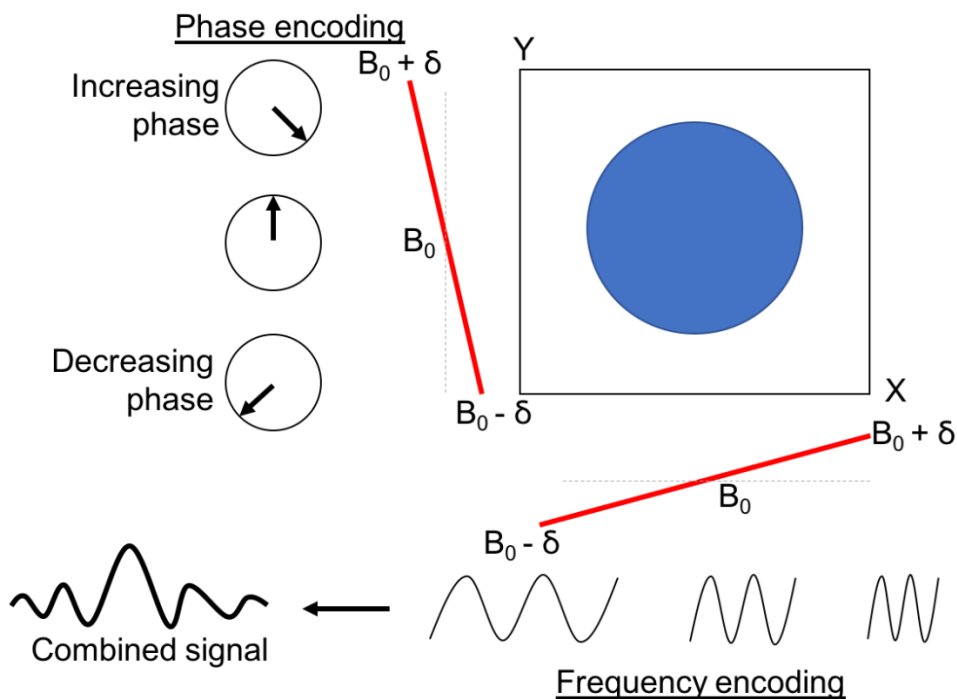


[Figure 2.5](#): The different encoding methods are depicted above. The phase accumulation or decrement is ruled by [Equation 2.27](#) differentiating in the x direction. Whereas the x direction is governed by the frequency encoding, with its signal given by [Equation 2.28](#). Figure adapted from [5]

2.2.3 *k*-Space and Image Reconstruction

The combination of frequency and phase encoding gradients fills the k-space, the Fourier-homologous space representing spatial frequencies. These frequencies are denoted by \mathbf{k} and are denoted by:

$$\begin{aligned}\mathbf{k}_{\text{FE}} &= \begin{cases} \gamma \int_0^t \mathbf{G}_{\text{FE}}(\tau) d\tau \doteq \gamma \mathbf{G}_{\text{FE}} t, & \text{FID signal,} \\ \gamma \int_0^t \mathbf{G}_{\text{FE}}(\tau) d\tau \doteq \gamma \mathbf{G}_{\text{FE}}(t - TE), & \text{echo signal,} \end{cases} \quad (2.29) \\ \mathbf{k}_{\text{PE}} &= \gamma \int_0^{T_{\text{PE}}} \mathbf{G}_{\text{PE}}(\tau) d\tau \doteq \gamma \mathbf{G}_{\text{PE}} T_{\text{PE}}.\end{aligned}$$

Derived from Equations 2.27 and 2.28. Where we use $\cdot := G(t) = G$, to derive the k forms with the use of time dependent and non-time dependent gradients.

It is only natural then to change the frame of reference to the one along the axes of the encoding gradients \mathbf{G}_{FE} , \mathbf{G}_{PE} , \mathbf{G}_{SS} which go now along our chosen directions \mathbf{k}_x , \mathbf{k}_y , \mathbf{k}_z in the k-space.

How we order the k-space coordinates is called the sampling trajectory. Phase encoding and slice selection define the initial points of the sampling trajectory, whereas frequency encoding may traverse the k-space freely. Some of the most used acquisition trajectories are:

- **Rectilinear/Cartesian:** When the k-space is filled line by line in the directions of the main k axes.
- **Radial:** When each trajectory goes through the center of the k-space and in radial direction.
- **Spiral:** When the trajectory resembles a spiral starting from the center of the k-space and unfolding into higher frequencies.

2.2.4 Imaging Sequences

To acquire the signal there are different methods to manipulate the transverse magnetization to have different contrasts on the image and to maximize the signal to noise ratio that can be measured by an acquisition. These techniques are called sequences and are divided into Spin Echo sequences and Gradient Echo Sequences.

2.2.4.1 Spin Echo Sequences

To counteract the dephasing of spins two consecutive RF pulses are used where typically the first one excites the bulk magnetization into the transverse plane and the second refocuses the spins by inverting the accumulated phases.

The most commonly used pulses are the excitation pulse 90° followed by an inversion pulse 180° pulse. After the excitation pulse, an appropriate waiting time, called echo time (TE), is used before acquiring the signal for the spins to be refocused. To acquire the next signal a time between excitation pulses is let by which is called repetition time (TR), to repeat the sequence.

Both times need to be tailored to the specific use case. If we want a higher T_1 recovery between acquisitions a longer TR is needed, whereas depending on the studied anatomy/tissue a different TE may be used. The only rules are that TR needs to be bigger than TE and that the distance between excitation and inversion pulse to be $t = \frac{TE}{2}$ for it to be a *complete* refocusing at acquisition time.

Because the spins are refocused at TE phase differences due to static field inhomogeneities ΔB_0 are removed, this is depicted in [Figure 2.6](#), here the signal experiences a T_2 decay since inhomogeneities are removed. Thus, the measured signal is governed by:

$$S_{SE} = S_o \cdot e^{-\frac{TE}{T_2}}. \quad (2.30)$$

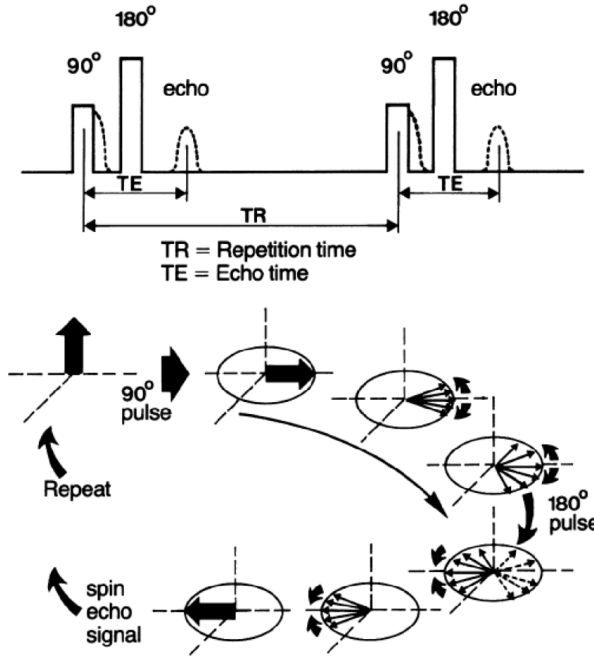


Figure 2.6: Spin echo sequence, and spin echo formation. A 90° ($\frac{\pi}{2}$) pulse excites the spins into the transverse plane. Following, the spins dephase and accumulate phase over a period of time $\tau = \frac{TE}{2}$. Then, a 180° (π) pulse inverts the accumulated phases. Finally, the spins rephase and form an echo at $t = 2\tau = TE$. Figure adapted from [35]

2.2.4.2 Gradient Echo Sequences

Instead of having an inversion pulse, one can make use of the phase accumulation during gradient excitation to produce a gradient echo.

Without loss of generality let's apply an excitation pulse of 90° and denote the accumulated phase of the transverse magnetization as Φ . Now let's apply two gradients in sequence: the first (negative) gradient G_- for a time-span T_- and second the gradient (positive) G_+ with the same magnitude as the negative gradient, with a start time T_+ and a finishing time t to be defined. Now the accumulated phase will be:

$$\Phi(r, t) = \gamma \int_0^t \mathbf{G}(\tau) \cdot \mathbf{r} d\tau = \gamma \mathbf{r} \cdot (G_- T_- + G_+ (t - T_+)) . \quad (2.31)$$

Since $\mathbf{G}_+ = -\mathbf{G}_-$, the accumulated phase becomes 0 at $t = T_- + T_+$ refocusing the bulk magnetization and generating an echo, in this case a gradient echo, since its cause by the gradients.

For the gradient echo signal we do not need to impose rules on the echo time TE since the magnitude, time and directions of the gradients are chosen freely. Although, TR and the gradients must be tailored to the specific needs depending on anatomies, tissue properties and hardware limitations.

Because the echo is caused by gradients we have an FID signal, hence, T_2^* decay is present and the signal is ruled by:

$$S_{GE} = S_0 e^{-\frac{TE}{T_2^*}}. \quad (2.32)$$

This sequence is depicted in [Figure 2.7](#)

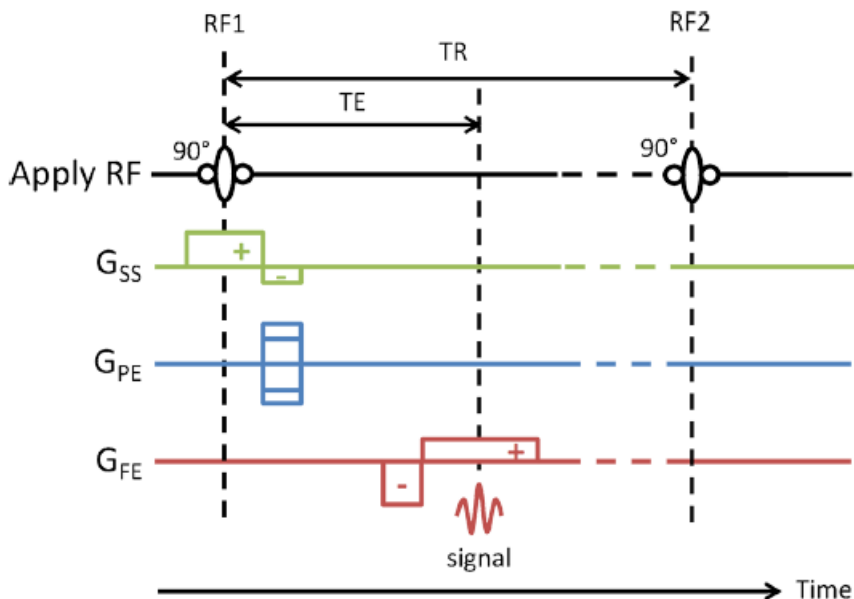


[Figure 2.7](#): Gradient echo sequence. A 90° ($\frac{\pi}{2}$) pulse excites the spins into the transverse plane, and the slice selection gradient is also applied. The phase encoding is done as normal and the gradients in the frequency encoding direction are chosen such that at time TE we capture an echo signal. Figure from [\[29\]](#)

2.2.5 Image reconstruction

Because we work with band-limited RF pulses we need to sufficiently fill the k-space to correctly sample the signal. The Nyquist-Shannon theorem states that for band-limited signals, the condition for optimal reconstruction is when the sampled measurements are at points spaced by the intervals not exceeding the inverse twice signal band width $\Delta x \leq \frac{1}{2\Delta f}$. The frequency that fulfills this condition $f_s = \frac{1}{\Delta x} \geq 2\Delta B$ is called Nyquist frequency.

Applying the theorem to Cartesian MRI with W_x, W_y representing the FOV we get the minimal k-space steps requirements:

$$\Delta k_x \leq \frac{1}{W_x}, \quad \Delta k_y \leq \frac{1}{W_y}, \quad (2.33)$$

2.2.5.1 Reconstruction

Because of gradient encoding techniques it derives that the time varying MR signal is the Fourier transform of the magnetization, hence, a discrete inverse Fourier Transform is needed to reconstruct the image from the k-space to the image-space. In the case that the image is not rectilinear the data needs to be re-sampled, or other special reconstruction techniques may be used.

If we use multi-coil acquisition the channel images need to be combined. For example as the sum of squares, ignoring the phase information:

$$I(\mathbf{r}) = \sqrt{\sum_c \frac{|I_c(\mathbf{r})|^2}{\sigma_c^2}}, \quad (2.34)$$

where σ_c^2 is the noise covariance of the coil.

WATER-FAT MRI

This part focuses the techniques for water-fat imaging in MRI are studied. The first section focuses on the main theory of the water-fat separation, following with the different techniques used in water-fat MRI and its limitations.

WATER FAT MRI

Fat contributes a significant MR signal in diagnostic imaging, it often requires either its suppression or separation from water-containing tissues to accurately quantify MR properties in mixtures with varying chemical shifts. When imaging short- T_2 tissues, it is often crucial to suppress signals from other long- T_2 water-containing tissues to enhance the contrast and clarity of the short- T_2 tissues. Furthermore, fat must be considered in the evaluation of tissue water properties, such as proton density, especially when partial volume effects are present.

Water-fat separation in MRI is essential for assessing metabolic disorders such as obesity, metabolic syndrome, and type-2 diabetes. The technique provides insights into body fat distribution and helps derive bio-markers like the Proton Density Fat Fraction (PDFF). [3, 9]

In water-fat imaging the acquisition is fitted onto a signal model, which describes the signal as the sum of water and fat components wrapped around common perturbation terms, such as background phase contributions.

3.1 CHEMICAL SHIFT ENCODING (CSE)

Chemical shift encoding (CSE) leverages the resonance frequency differences between water and fat protons to separate their signals. Water-Fat acquisitions are used to encode these differences, enabling the separation of water and fat signals into distinct images.

Signal Model

To separate the water and fat from the image we work with a multi-peak signal model, which considers two main nuclei: water and fat nuclei. Water is composed by a single frequency, which we assume to be at zero in the rotating frame of reference, whereas fat has multiple peaks at different frequencies depending on the chemical structure that the hydrogen nucleus is bound to.

The assumption is made that the relative frequency shifts and amplitudes between fat peaks are known and constant. One example of an MR spectrum is depicted in [Figure 3.1](#).

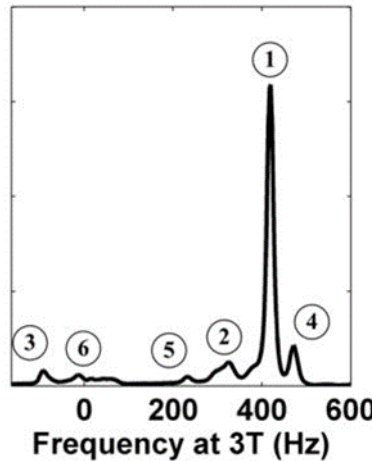


[Figure 3.1](#): Fat spectrum of an MR scan. The spectra were shifted and displayed such that the main fat peak is at 420 Hz relative to water. The spectrum depicts a multi-peak pattern. Six peaks can be identified, and their chemical shift frequencies relative to the water resonance frequency at 3T are labeled. Image adapted from [\[37\]](#)

Thus the signal model for a specific voxel at time t with a fat spectrum $c(t)$ with P fat peaks, relative amplitudes α_p and relative phase shifts Δf_p , in addition to a local bulk frequency shift ψ_{bulk} due to field inhomogeneities. All peaks, including water, are assumed to decay with the relaxation rate R_2^* . Hence, the signal can be represented as:

$$S_{raw}(t) = (W + c(t)F)e^{\psi_{bulk}(t) - R_2^*t}$$

where: $c(t) = \sum_{p=1}^P \alpha_p e^{2\pi i \Delta f_p t}$, with $\sum_{p=1}^P \alpha_p = 1$, (3.1)

where water and fat are denoted by W and F respectively. Ψ_{bulk} is composed of off-resonance effects due to B_0 inhomogeneities and B_1 transmit/receive phases. When using multi-echo techniques the B_1 effect can be mitigated, its effect is not time dependent and by simple subtraction of two echos the transmit/receive phase can be taken out.

3.2 MULTI-TE DIXON IMAGING

The original water-fat separation algorithm developed by Dixon relied on acquiring two echo times, and is known as "two-point Dixon" [8]. This technique separated water and fat by acquiring one image when the fat and water signals are in-phase (IP) ($c_1 = +1$) and one image when water and fat are out-of-phase (OP) ($c_2 = -1$), where c_1, c_2 refer to the first and second echo time respectively. Because of the multi-echo addition and subtraction one can assume that only the B_0 effects are zero, since B_1 and other time dependent effects are mitigated by the linear combination of the signal. Hence, assuming $\Psi_{bulk} = 0$, a single fat peak model, and neglecting R_2^* decay effects, water and fat can be separated by adding and subtracting the IP and OP MR images. However, due to the absence of field map terms in the original two-TE Dixon method, water-fat separation becomes problematic in regions with significant B_0 field inhomogeneities.

The three-TE Dixon technique was introduced to address B_0 field variations, requiring three TEs acquired at IP and OP TEs [11]. The off-resonance induced phase map is calculated and used to generate water and fat-separated images. Similarly, in an extended two-TE technique, the magnitude-based method is replaced by using the complex IP and OP images, allowing the calculation of the off-resonance induced phase map [33]. By accounting for Ψ_{Bulk} , both the three-TE Dixon and extended two-TE Dixon methods enhance the accuracy of fat-water separation [16]. While estimating the field map improves water-fat separation image quality, water-fat swaps can occur in regions with significant phase variations due to B_0 field inhomogeneity. Beyond the two-TE and three-TE Dixon methods, alternative approaches have been proposed to solve the water-fat problem, which is a non-convex non-linear problem due to the field map term.

To enhance fat-water separation in the presence of B_0 field inhomogeneities, Dixon water-fat separation methods have been combined with commonly used phase unwrapping techniques such as region growing [6, 36], polynomial fitting [38], and solving Poisson's equations [34]. These phase unwrapping methods assume that the B_0 field varies smoothly across the image [16]. Since the fitting problem has multiple local minima, the solution for the field map in the water-fat separation problem depends on the initial guess [7]. Advanced complex fitting algorithms, are needed to improve field map estimation, par-

ticularly in regions with low signal to noise ratios (SNRs) or rapidly varying fields where water-fat swaps might occur. [22]

3.3 SINGLE-TE DIXON IMAGING

Single-TE Dixon methods decompose fat and water components from a single complex MR image [8]. These methods have shorter acquisition times than multi-TE methods, since only a single complex image is acquired, making them suitable for dynamic imaging. In the original single-echo Dixon method, data is acquired with fat in the imaginary channel and water in the real channel by choosing a TE when the phase between water and fat components is $\theta(t) = \angle c(t) = \frac{\pi}{2}$.

When the echo time is short, we can neglect the T_2^* decay effects. Thus, the signal can be expressed as:

$$S_{Raw}(t) = (W + c(t)F)e^{i\phi_{bulk}(t)} \quad (3.2)$$

where ϕ_{bulk} represents all phase terms common to both water and fat, including contributions from spatially dependent B_0 field inhomogeneities, eddy currents, signal delays in the receiver chains, and B_1 transmit/receive phase effects [16]. Assuming $\phi_{bulk} = 0$, water and fat can be estimated from the real and imaginary parts of the signal as:

$$\begin{aligned} F &= \frac{\text{Im}(S(t))}{\sin \theta(t)} \\ W &= \text{Re}(S(t)) - F \cos \theta(t) \end{aligned} \quad (3.3)$$

Optimal noise performance is achieved when the relative phase of water and fat signals is $\frac{\pi}{2}$, since it is when they are completely separated into the imaginary and real channel.

In practice, the assumption of an homogeneous B_0 field map is not valid, and pre-calibration of the field map (e.g., using multi-TE Dixon) is required. Different techniques have been reported to remove unwanted phase terms, including additional reference scans [8], region-growing algorithms to estimate unwanted phase terms [16], and solving the smoothness-constrained inverse water-fat problem directly [21]. Acquiring additional reference scans increases scan times and introduces potential errors due to patient motion and other

inconsistencies. Thus, a balance between acquisition time and separation quality is needed, which requires calibration.

ULTRA SHORT ECHO TIME IMAGING (UTE)

This section focuses on Ultra Short Echo Time Imaging (UTE) for imaging short T_2/T_2^* tissues.

ULTRA SHORT ECHO TIME IMAGING (UTE)

Tissues such as cortical bone, tendons, ligaments and menisci, which have a short T_2 , provides useful information and contrast to recognize abnormalities that produce an increase in signal.[31]

Using basic spin echo sequences with $TE = 10 - 20$ ms, tissues with T_2 s shorter than 10 ms prove not to be detectable[15]. However, with shorter TEs of around 1 – 2 ms using gradient echo pulse sequences, the detectability increases to tissues with T_2 s of 1 – 2 ms.[31]

Pulse sequences with even shorter echo times are called ultra short echo time (UTE) sequences. These echo times are commonly 100 – 1000 times shorter than those of conventional sequences used for imaging short- T_2 tissues in the musculoskeletal (MSK) system [31].

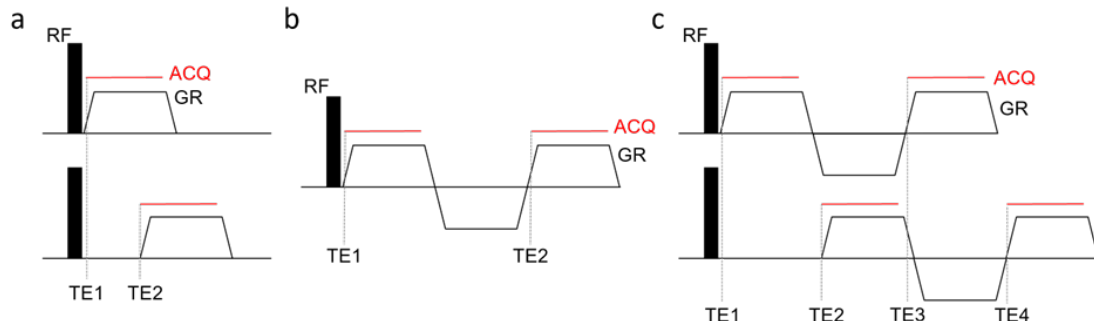
4.1 IMAGING SHORT T_2 TISSUES

To image short- T_2/T_2^* tissues, ultrashort echo time (UTE) techniques are used. There exist two main methodologies for UTE Dixon sequences: multi-echo UTE sequences and single-echo UTE sequences, both have their advantages and disadvantages, both sequences are depicted in [Figure 4.1](#).

Multi-echo sequences as presented in [Figure 4.11](#) use more than one echo to generate and enhance the contrast for short T_2 tissue. This is specially effective for suppressing long and medium T_2 signals to enhance contrast of short- T_2 components, because the signal of short T_2 tissues at the time of the next echo decreases significantly and is not affected by the subtraction of the signals. However, the need of multiple echoes lengthens the acquisition time.

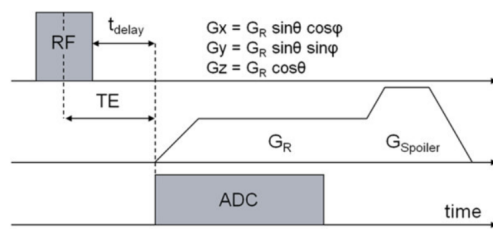
In contrast, single-echo sequences, as depicted in [Figure 4.12](#), use only one echo to generate the signal. As described above, since the echo times are very brief for UTE short T_2 tissues can be detected by the acquisition. This permits obtaining the contrast directly from the first acquired signal. Although, if the

focus is high contrast for short T_2 tissues, using multi-echo delivers a higher contrast to noise ratio (CNR)



1. Multi-echo UTE methodologies. (a) Multi-acquisition for a dual-echo sequence: multiple TEs are acquired in consecutive iterations. This approach provides significant flexibility in choosing TEs, but at the expense of scan time efficiency. (b) Multi-echo for a dual-echo sequence: several gradient echoes are captured during each iteration, enhancing scan time efficiency relative to the multi-acquisition UTE. However, the requirement for optimal TEs for further processing (such as Dixon imaging) imposes constraints on how the TEs need to be selected, also constrains the spatial resolution of the sequence. (c) Interleaved multi-echo UTE : this technique integrates the multi-echo and multi-acquisition UTE strategies. Multiple echoes are obtained in each sequence repetition, and the TEs are varied across acquisitions, allowing for more flexible TE selection while retaining the increased scan time efficiency of the multi-echo method. Adapted from [22].

$$\begin{aligned} \text{TE} &= t_{RF}/2 + t_{\text{delay}} = 70 \mu\text{s} \\ t_{RF} &= 60 \mu\text{s} \\ t_{\text{delay}} &= 40 \mu\text{s} \end{aligned}$$



2. Single echo UTE sequence: (a) Depiction of the single echo UTE sequence. The direct acquisition of the signal benefits of faster scan-times, making the sequence suitable for dynamic imaging. ADC is the analogue to digital converter (ADC) of the signal, $G_{x,y,z}$ the orthogonal gradients and G_R and G_{Spoiler} the readout and spoiler gradients, respectively. Figure adapted from [28].

Figure 4.1: UTE Imaging Sequences.

SINGLE ULTRA SHORT ECHO TIME DIXON IMAGING (SUTE-DIXON)

In this chapter we concentrate on the novel technique presented by Kronthaler S. [21], as an iterative approach to solve the water-fat separation problem in an inverse manner. The advantages and limitations are discussed, and possible solutions are mentioned as a motivation for further analysis.

SINGLE ULTRA SHORT ECHO TIME DIXON IMAGING (SUTE-DIXON)

5.1 THE STUDY

An alternative method, introduced by Kronthaler et al. [21], eliminates the necessity for an additional B_0 calibration by addressing the issue as a smoothness-constrained non-linear inverse water-fat problem. Their findings indicated that at ultrashort echo times (UTE) of less than 0.14 ms at 3 T, phase contributions from B_0 inhomogeneities are minimal due to the brevity of the TE. These B_0 contributions arise from sources such as magnet inhomogeneity, shim fields, object-based susceptibility, and residual background field effects [7].

It is important to note that the UTE phase includes a significant B_1 phase component that varies gradually in the axial plane and predominates in UTE phase maps with TE = 0.14 ms during lumbar spine imaging at 3T. The B_1 phase, resulting from the tissue's electric conductivity, exhibits a roughly parabolic shape as described by Maxwell's equations [18, 20, 24].

The studied approach assumes that the unwanted phase terms are predominantly due to the B_1 phase, which varies smoothly across the field of view (FOV) and is thus managed using a smoothness constraint. Their research, involving patients with lumbar spine vertebral fractures, demonstrated that this methodology effectively removed unwanted low-frequency background phase and successfully separated water and fat signals using a single-echo UTE image. This technique allowed for simultaneous evaluation of vertebral fractures and edema in the thoracolumbar spine using a single MR sequence. In an extended study, the method was tested across different anatomical regions, on two separate scanners, with various coils and different TEs.

The study achieved an accurate depiction of short T_2 components and effective water-fat separation. Significant B_0 inhomogeneity variations in the cervical spine were successfully corrected. For knee scans, a transmit-receive coil

was utilized, resulting in a different B_1 transmit-receive phase compared to receive-only coils. Despite this added complexity, the method delivered high-quality water and fat-separated images. The approach's advantage lies in its ability to eliminate unwanted phase terms, whether arising from B_0 or B_1 , without requiring an additional calibration scan. The post-processing is fully automated, offering a significant improvement over filtering methods that necessitate specifying kernel size and filter type for each subject.

5.1.1 *The iterative optimization method*

Under the assumption, that the background phase consist primarily of the B_1 phase, which is a smooth phase varying over the FOV, the proposed non-linear inverse background-phase problem is proposed:

$$\begin{aligned} \phi^* &= \underset{\phi}{\operatorname{argmin}} \kappa(\phi) \\ &= \underset{\phi}{\operatorname{argmin}} \frac{1}{2} \left\| (W + F e^{i\theta(TE)}) e^{i\phi} - S_{Raw}(TE) \right\|^2 + \lambda \|M \nabla \phi\|^2, \end{aligned} \quad (5.1)$$

where we introduce the variables ϕ^* as the optimal solution for the background phase estimation, λ as the regularization hyper-parameter for the smoothness constraint, M as the mask which constraints the image up to the anatomy borders and ∇ as the 3D gradient operator.

To solve the problems we linearize the cost function for a small update $d\phi$:

$$\begin{aligned} \kappa(\phi + d\phi) &= \\ &\frac{1}{2} \left\| (W + F e^{i\theta(TE)}) e^{i\phi} (1 + id\phi) - S_{Raw}(TE) \right\|^2 + \lambda \|M \nabla(\phi + d\phi)\|. \end{aligned} \quad (5.2)$$

Since we are dealing with a convex function the optimal update $d\phi$ may found by solving:

$$\begin{aligned} 0 &= \frac{\partial}{\partial \phi} \kappa(\phi + d\phi) \\ d\phi &= -\operatorname{Im}((W + F e^{i\theta(TE)}) e^{i\phi} S_{Raw}^H(TE)) - 2\lambda \nabla^H M^2 \nabla \phi. \end{aligned} \quad (5.3)$$

After we found a good approximation of ϕ we can calculate the water and fat components from the filtered signal $S_{filter} = S_{Raw} \cdot e^{-i\phi^*}$ as follows:

$$\begin{aligned} F &= \frac{\text{Im}(S_{filter})}{\sin(\theta(TE))} \\ W &= \text{Re}(S_{filter}) - F \cos(\theta(TE)) \end{aligned} \quad (5.4)$$

The algorithm is as follows:

Algorithm 1 Gaussian Iterative Optimization

```

1: UTEphase  $\leftarrow$  Unwrap( $\angle(S_{raw})$ )
2:  $M \leftarrow$  getFilledAnamotyMask(UTEphase)
3:  $W_0, F_0, \phi_0 \leftarrow 0, 0, 0$ 
4: procedure GAUSSIAN OPTIMIZATION( $\lambda, S_{Raw}, W_0, F_0, \phi_0, M$ )
5:   while  $\frac{\|d\phi_n\|}{\|\phi_n\|} \leq 0.01$  do
6:      $d\phi_n \leftarrow$  Equation 5.3
7:      $\phi_{n+1} \leftarrow \phi_n + d\phi_n$ 
8:      $S_{filter} \leftarrow S_{Raw}e^{-i\phi_{n+1}}$ 
9:      $W_{n+1}, F_{n+1} \leftarrow$  Equation 5.4
10:   end while
11:   return  $\phi^*, W^*, F^*$ 
12: end procedure
  
```

To prevent phase wraps during the update steps, the phase was scaled to be between $-\pi, \pi$. The tissue mask is used in the regularizer to only perform the water-fat separation in areas with tissue components. This also prevents errors due to the sudden increase at the anatomy edges and section from signal to no-signal regions where the derivative becomes very large.

5.1.2 Limitations and Motivation

Although the results encountered in [21] are promising, they don't come without limitations.

First, the assumption of the B_0 and B_1 relative contributions are not tested empirically, hence, there is no certainty on when and where we can neglect certain effects, specially B_0 effects, as is done in the study. Moreover, if we need to account for B_0 modeling as it was done in previous studies as described in Chapter 3.

Second, [Equation 5.2](#) is inherently ill-posed since we have 3 variables W, F, ϕ for only two linear independent equations. Without proper initialization the robustness of the model may not be as good as it can, and can derive in unexpected behavior since we have multiple *correct* convergence paths.

Thus, this study focus on addressing this two points and studying different techniques on how to achieve a better performance and robustness on the presented model.

THESIS FOCUS: TOWARDS A ROBUST SINGLE ULTRA SHORT ECHO TIME DIXON IMAGING

This section focuses on testing experimentally if B_0 and B_1 are the main contributions in the background phase of sUTE Dixon Imaging. Answering the question allows better modeling and the for more efficient removal of the background phase.

THESIS FOCUS: TOWARDS A ROBUST SINGLE ULTRA SHORT ECHO TIME DIXON IMAGING

6.1 BACKGROUND PHASE CONTRIBUTIONS

In single-point UTE Dixon (sUTE Dixon) there exists multiple background phase contributions that prove detrimental to the water-fat separation quality. The magnetic fields B_0 and B_1 as well as Eddy currents and signal delays to the receiver coils contribute to the distortion of the phase of an otherwise plain MR acquisition. This study focuses on the B_0 and B_1 phase contributions which arises from their respective magnetic fields and have different causes.

For once the B_0 field inhomogeneities come from the main magnetic field, which means that gradient-echo (GRE) sequences are more vulnerable to this effects than spin-echo (SE) sequences because of the FID[10], but also has the advantage that shimming coils were developed specifically to reduce the effects of B_0 field inhomogeneities.

This contributions take the form:

$$f_B = \gamma(\Delta B_0 + B_{shim} + B_\chi + \delta), \quad (6.1)$$

with B_{shim} being the shim field, B_χ is the field-map estimate and δ some residual field. [7]. Focusing on the B_0 contribution one can model it by using a sum of spherical harmonics:

$$\Delta B_0(\mathbf{r}) = \sum_{\ell=1}^L \sum_{m=-L}^L C_{\ell m}^{\Delta B_0} Y_{\ell m}(r, \phi, \theta), \quad (6.2)$$

and the spherical harmonics can be approximated as a standard polynomial. An alternative to this is to model it via a dipole kernel approximation as in [32] with:

$$\varphi_{B_0}(x, y, z) = -\gamma B_0 TE \cdot \mathcal{F}^{-1} \left[\left(\frac{1}{3} - \frac{k_z^2}{K^2} \right) \cdot \mathcal{F}(\chi(x, y, z)) \right], \quad (6.3)$$

where χ is the field map of the object and \mathcal{F} is the Fourier Transform. For analyzing the field effects [Equation 6.3](#) is used.

For the B_1 field inhomogeneity it behaves as a local effect, it generates from the transmitter/receiver field and depends on the conductivity of the tissue, which means that borders between very distinctive tissues have high distortions due to the B_1 effect. This phase as discussed in [3](#) is a slowly varying phase with a polynomial envelope, which hints us to use a plain polynomial fit to study the effect.

6.1.1 Experiments

The goal is to measure B_0 and B_1 and its effect on the water fat separation in a controlled manner. To achieve this, we need a phantom with clear separate regions of water and fat where their conductivity and hence, B_1 inhomogeneities can be modified in a controlled manner. For this, an oval container is filled with three parts water and one part oil and the $B_1 \& B_0$ maps are measured. One measurement is made with plain water and oil, and the second measurement is measured with oil and water with added salt to increase conductivity. A thoracic coil was used to scan the phantom and enhance the signal. The phantom is depicted in [Figure 6.1](#).

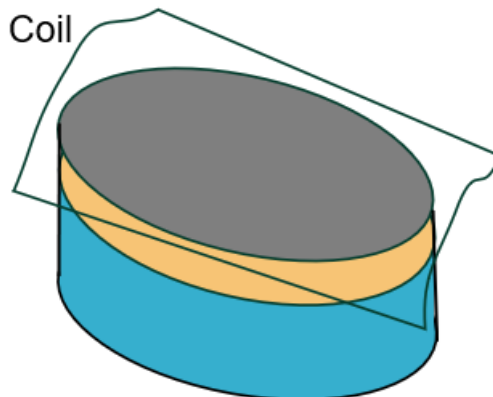


[Figure 6.1](#): The phantom. Three parts of water to one part of oil was mixed. To avoid velocity effects it was let to rest for a couple of minutes before scanning. A thoracic coil is used to enhance the signal

Three scans were performed. A normal sUTE scan, and two scans to measure the B_1 effect and the B_0 effect separately. For the B_1 scan the dubbed dual

refocusing echo acquisition mode (DREAM) is used [27], for the B_0 mapping we used a three-echo Dixon.

This three scans were performed twice: once with plain water, and once with salt added to increase conductivity. To further improve the study validity the UTE scans were performed without shimming to clearly observe the B_0 contribution at its fullest.

The resulting unwrapped UTE phase for both cases is depicted at Figure 6.2 all phases are depicted in [rad] unless stated otherwise. The image for the plain water a) is as expected with a *constant* phase throughout the species, as well as in fat. When salt is added b) the conductivity of water increases, but the fat phase continues the same as salt does not mix with fat, this can be seen in the image from the visual smooth curvature that water presents from inner to outer image, which supports the idea that B_1 is first smoothly varying, and second can be reasonably approximated by a smooth function.

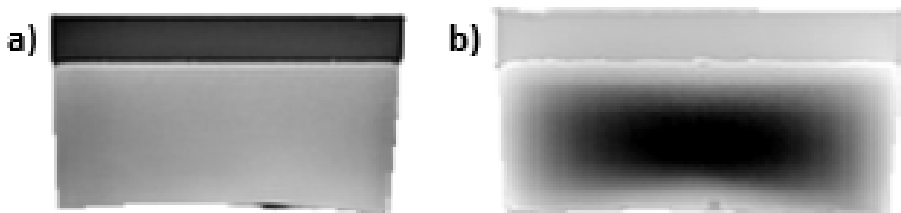


Figure 6.2: a) UTE unwrapped phase for phantom without added salt. A smooth plain phase can be seen from the image in the water and fat regions. b) Phase for phantom with added salt. A polynomial variation of the phase can be seen from the image in the water region due to higher conductivity because of the salt. The inner part of the object has a greater effect than the outer part.

6.1.2 B_0 effect

To fit the background phase contributions we use the kernel dipole approximation Equation 6.3 for B_0 , which we call forward model. We compare the results from the dipole approximation to the measured B_0 . Note that B_0 only needs to be modeled once, since the addition of salt does not affect the main field. See Figure 6.3

The B_0 phase is small, which may reduce its effect on the overall impact on the signal. To test the effect the fit is filtered out separately from the UTE phase, with the resulting filtered UTE phases are depicted in Figure 6.4.

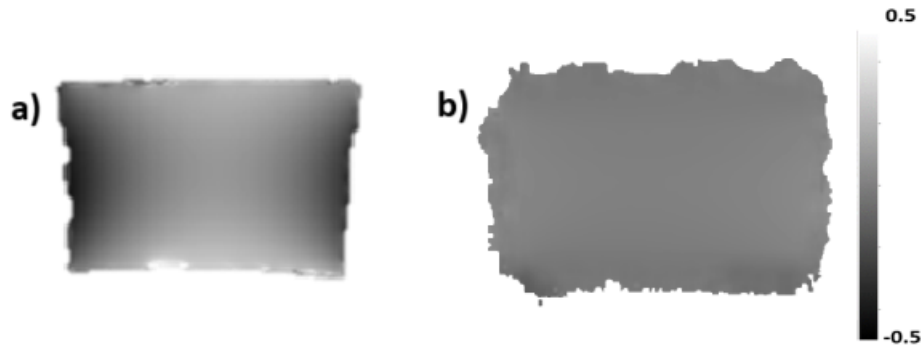


Figure 6.3: B_0 phases for the phantom. a) The B_0 modeled phase done via [Equation 6.3](#). b) Measured B_0 . The values of the B_0 phase are small in comparison with the UTE phase ranging from (-0.5, 0.5) rad.

The B_0 filtered phase in [Figure 6.4](#) show no noticeable difference with the original phase images [Figure 6.2](#). As mentioned This validates lightly the assumption that B_0 may not be the driving phenomenon for the background phase contributions.

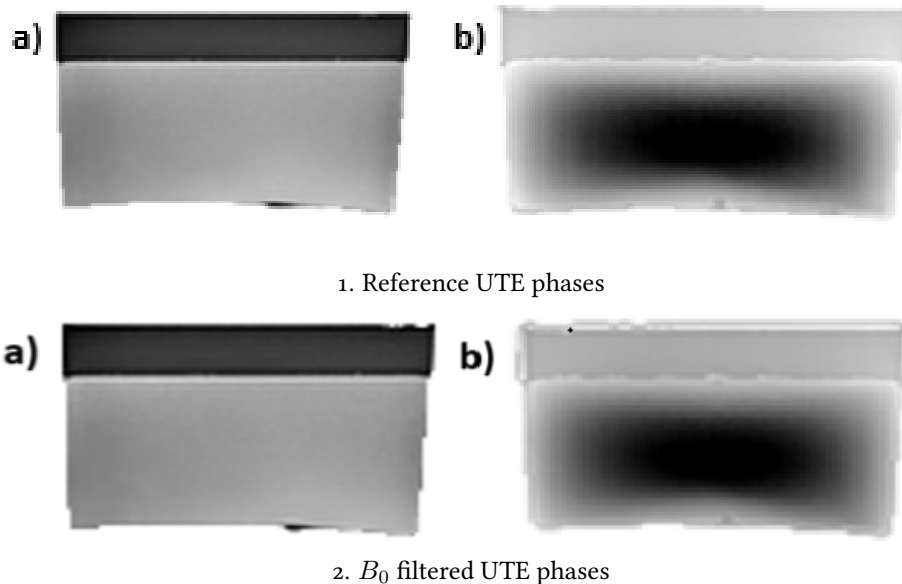


Figure 6.4: 1. Reference UTE phase, 2. B_0 filtered UTE phases for the phantom with a) and without b) added salt. The B_0 modeled phase was subtracted from the phase. a) & b): There is no noticeable difference between the reference phases (1.) and the images here. This lightly supports the assumption that B_0 field inhomogeneities is not the driving background phase phenomenon.

6.1.3 B_1 effect

To further study the phantom the B_1 effect is modeled. A second-degree 3D polynomial fit was chosen because of the smoothly varying properties of B_1 and its distinct curvature resembling a 3D convex polynomial. See [Figure 6.5](#)

The polynomial fit is conducted restricted on the water, since fat is only lightly affected by B_1 field inhomogeneities, and salt does not mix with fat in order to increase its conductivity. This fit is then filtered from the signals to compare its effect on the resulting filtered phase. It's important to note that, in this case, the addition of salt does impact on the B_1 measurements since they depend on the conductive nature of the species to be analyzed. See [Figure 6.6](#)

The B_1 maps show smoothly varying phase with convex curvatures as expected. A quantitative comparison is difficult since the DREAM method [27] calculates the relative shift of the flip angle from B_1 inhomogeneities, this cannot be *quantitatively* compared raw to the derived phase from the fit, but a *qualitative* comparison is possible, from which the correctness of the modeling can be inferred as in this case.

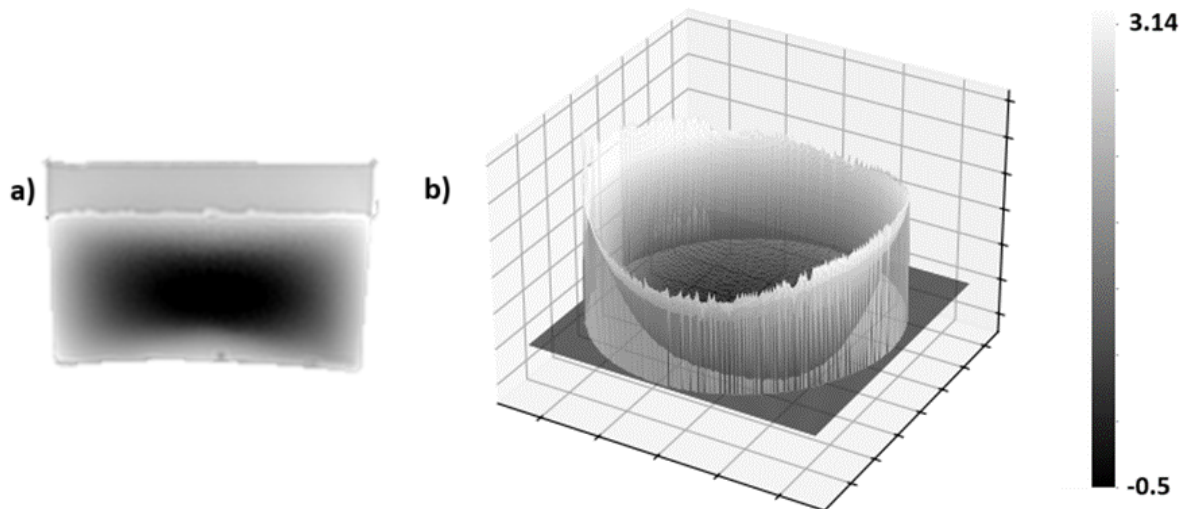
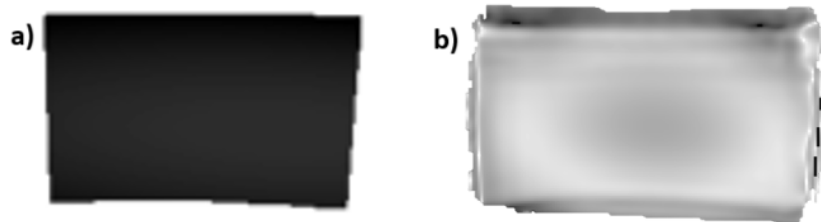


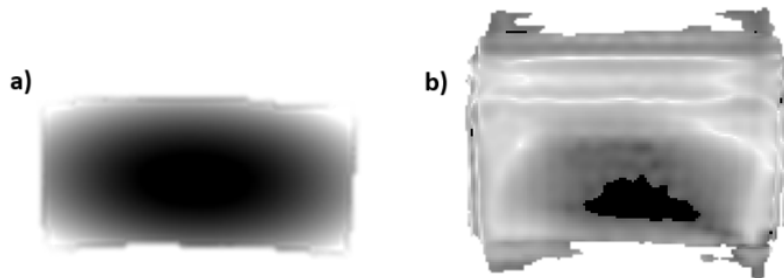
Figure 6.5: a) UTE unwrapped phase for the phantom with added salt. b) Surface plot of the UTE phantom slice. The phase of the phantom in the water species resembles an even 3D polynomial. Which supports the approach of using a second-degree 3D polynomial fit for modeling the B_1 phase.

This phase is then subtracted from the signal to get S_{filter} . See [Figure 6.7](#). The effect are much more noticeable as the originating from B_0 , the fit corrects the image and makes it smoother, reducing the background phase originating from B_1 . This enables us to also reduce the contrast window, as done in the figure, which lets us see the, small, but not negligible impact that the fit has on the phase. For example, for the phantom without salt some slight curvature is present in the filtered image, which we can deduce, comes from the polynomial fit. For the phantom with added salt, although it reduces the *cupping* effect greatly it has some limitations at the edges of water.

At first glance, it is qualitatively shown that the B_1 effect has a greater effect on *flattening* the image than the B_0 effect when salt is added. For completeness the derived water-fat images are depicted in [Figure 6.8](#). The separation is correct, validating further the modeling method; the separation is smoother in the phantom without added salt, which is expected since the UTE-phase is also curved when salt is added. The contrast is also higher for the case with added salt, since salt spreads the water and fat phases further due to water conductivity as seen in [Figure 6.5](#).



1. B_1 maps for the phantom without added salt. Both images are smooth plain maps, that supports a good phase modeling.



2. B_1 maps for the phantom with added salt. Note that because only the water part was fitted, only the water species is depicted. Both B_1 maps deepen in the inner part of the water species, supporting a correct modeling of the phase.

Figure 6.6: a) Modeled [rad] and b) ground truth [% $\Delta\alpha$] B_1 maps of the phantom without salt.(1.) and the phantom with added salt (2.). **NOTE:** Its quantitative comparison is difficult since the DREAM method returns the percentage of change relative to the main flip angle, whereas the phase is modeled directly from the polynomial fit, and its conversion is not possible.

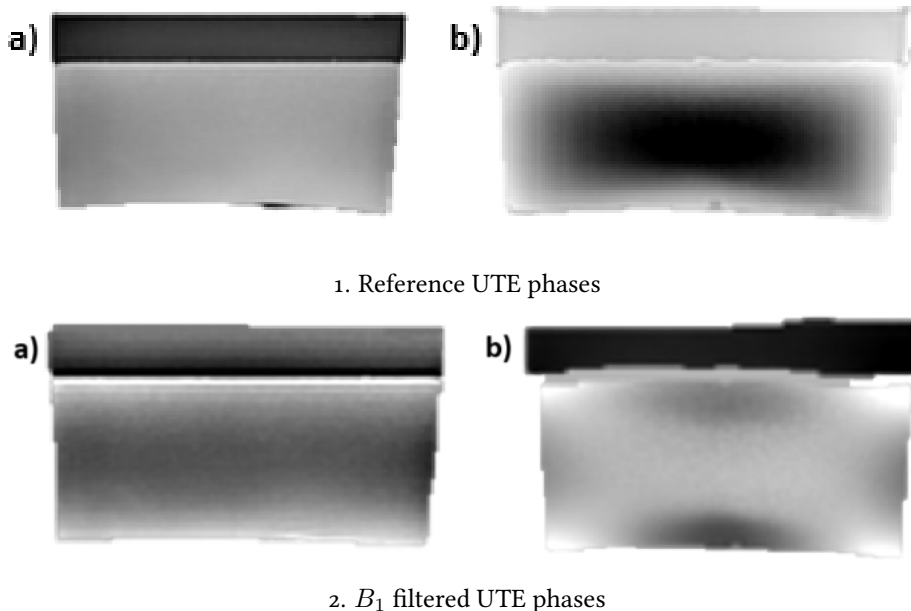


Figure 6.7: 1. Reference UTE phase, 2. B_1 filtered UTE phases. a) Phantom without salt. b) Phantom with salt. The images are smoother than the reference UTE phases (1.), specially in the phantom with added salt a great improvement is seen, but not without its imperfections, such as some artifacts at the phantom edges.

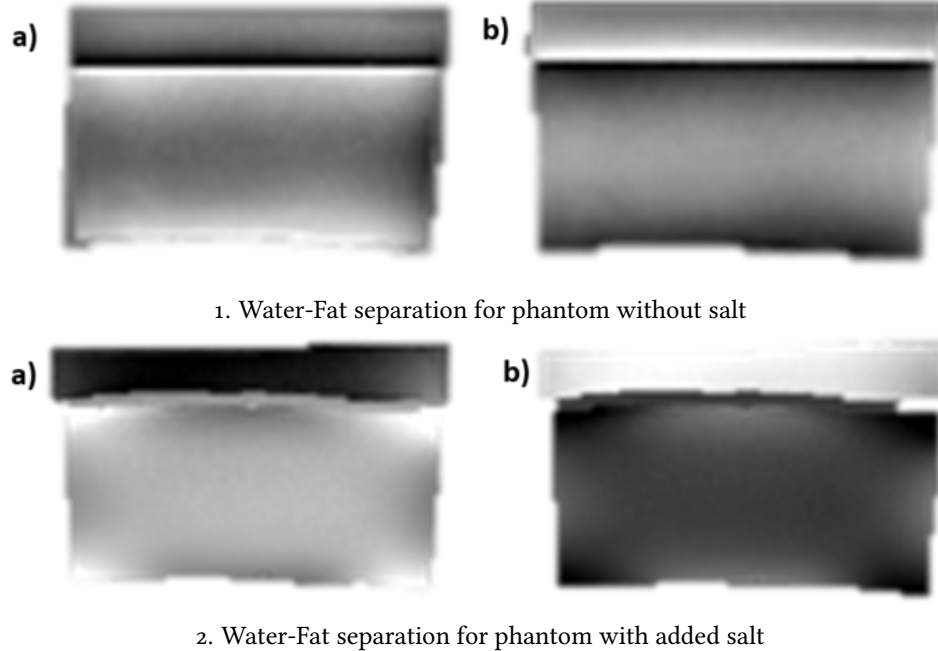
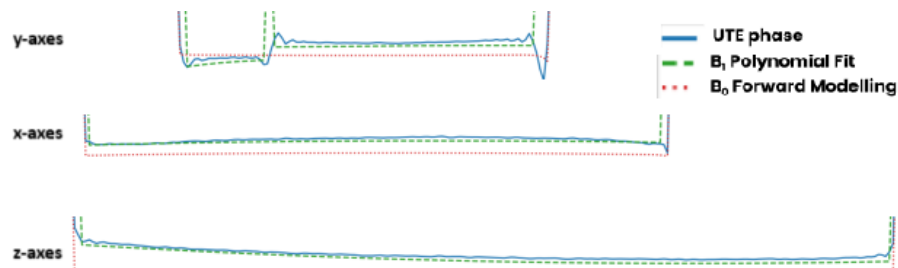


Figure 6.8: Water Fat separation. a) Water b) Fat. The separation is correct and much smoother in the phantom without added salt, as expected, because of the UTE-phase shape as depicted in the contour plot in Figure 6.5.

6.1.4 Quantitative Comparison

Having showed that the modeling techniques deliver acceptable results, one can further validate the relevance of the field inhomogeneities in the background phase contributions also when no salt is added, by quantitatively analyzing it. Since we first take a closer look into the UTE phase compared to the B_0 and B_1 modeled phases for a specific slice. For this lines are plotted through the two species of the phantom (water and fat) and the different phase contributions are compared. See [Figure 6.9](#)



1. Water line-plots, y-direction is the common direction that crosses both water and fat.



2. Fat line-plots

[Figure 6.9](#): Zoomed line-plots through water (1.) & fat (2.). It is shown how the curvature of the raw UTE phase cannot be correctly approximated by the forward modeled phase of B_0 . On the other hand the B_1 modeled phase with the 2nd degree 3D polynomial has no problem adapting to the slight curvature of the phase inside the phantom.

On the zoomed-in line-plots can be seen how the B_1 modeled phase fits the raw UTE-phase more appropriately, when the B_0 kernel dipole approximation lacks the flexibility to correctly fit the raw-signal.

To conclusively prove that the B_1 effect has a greater effect on the signal than the B_0 effect we measured the *flatness* of the filtered phase on both fat and water species by summing the gradients of both regions together and separately. The results are on [Table 6.1](#).

The sum of gradients measurements prove quantitatively that B_1 modeling indeed has a greater impact on the background phase than B_0 in both tissues water and fat as already stated by Kronthaler et al. [22].

Species	Modeled phase	Sum of gradients
All	B_0	1.037
All	B_1	0.148
Water	B_0	0.085
Water	B_1	1.191×10^{-7}
Fat	B_0	0.281
Fat	B_1	4.768×10^{-7}

Table 6.1: Flatness measurements for different regions of the phantoms filtered phase. The phase is filtered by subtracting the modeled B_0 and B_1 effects on the background phase of the signal. Note that the sum of gradients in done in species regions lightly smaller than the real area to avoid high spikes at borders. That is why the sum of gradient over the whole image is different than the sum of both water and fat sum of gradients separately.

This builds the foundation on what is critical to be modeled for initializing the ill-posed iterative optimization method in [Section 6.2](#).

INITIALIZATION OF THE ITERATIVE OPTIMIZATION METHOD IN CLINICAL APPLICATIONS

6.2 INITIALIZATION OF THE ITERATIVE OPTIMIZATION METHOD IN CLINICAL APPLICATIONS

Having analyzed the relevance of the field inhomogeneities effects on the background phase of the UTE scan in [Chapter 6](#), it is turn to tackle the second point made in [Section 5.1.2](#), where the importance of initializing the ill-posed Gaussian iterative optimization problem is highlighted.

The purpose of this chapter is to propose a new algorithm that model the field effects previously to the iterative optimization algorithm and to analyze the effects of such initialization in the water-fat inverse problem stated in [Equation 5.1](#) with the purpose of achieving a more robust method with respect to the regularization parameter λ and a better quality of water-fat separation.

6.2.1 *The Algorithm*

The idea behind the initialization algorithm is to give the convergence path of the ill-posed method the right starting point and hence the right direction till convergence. Since the solution space of [Equation 5.1](#) has many local minima, the method cannot guarantee that the global minima is achieved. Nevertheless, better initialization is bound to have better results.

The proposed algorithm is introduced in [Algorithm 2](#). The Limited-Memory Broyden–Fletcher–Goldfarb–Shanno Algorithm (L-BFGS) method is used, since the 3D images are normally spatially heavy. This method is a quasi-Newton second-order optimization method where a history of the past updates is maintained to attain the best possible convergence direction. The inputs of the method are the learning rate (lr), the gradient tolerance (gtol), the update tolerance (xtol) and the maximum number of iterations iterations. The error function to be minimized is given by:

$$f_{error} = \frac{1}{2} \frac{\sum_{i \in M} [M_i(y_{gt,i} - y_{pred,i})]^2}{|M|}, \quad (6.4)$$

$$y_{pred,i} = g(x_i),$$

where $g(x)$ is the function to be fitted to the background phase. For this case we choose an even degree 3D polynomial function, because of the shape of the background phase, see [Figure 6.5](#).

Algorithm 2 Gauss Newton with Initialization

```

1:  $UTEphase \leftarrow \text{Unwrap}(\angle(S_{raw}))$ 
2:  $M \leftarrow \text{getFilledAnamotyMask}(UTEphase)$ 
3: procedure PHASE MODELING INITIALIZATION( $lr, gtol, xtol, maxIter$ )
4:   Initialize the polynomial coefficients  $a_i \leftarrow \mathcal{N}(0, 1)$ 
5:    $f_{error} \leftarrow$  Equation 6.4
6:    $\phi_0 \leftarrow \text{L-BFGS}(f_{error}, \vec{a}, lr, gtol, xtol, maxIter)$ 
7:    $\hat{S} \leftarrow S_{raw} \cdot e^{-i\phi_0}$ 
8:    $W_0, F_0, \phi_0 \leftarrow$  Equation 5.4,  $\phi_0$ 
9: end procedure
10:  $\phi^*, W^*, F^* \leftarrow \text{Gaussian Optimization}(\lambda, S_{Raw}, W_0, F_0, \phi_0, M)$ 
11: return  $\phi^*, W^*, F^*$ 
  
```

The resulting W_0, F_0, ϕ_0 from the phase modeling are then input as the initial points to the Gaussian optimization algorithm, which are then used to produce the final phase, water and fat separation ϕ^*, W^*, F^* .

The algorithm is depicted in [Figure 6.10](#). The method uses a type of *pre-processing* of the signal before it gets input into the Gauss Newton method. This is divided into three parts:

1. The signal UTE phase is unwrapped and used by the polynomial fit to obtain the first guess of the background phase ϕ_{init} .
2. The filtered phase $S_{filtered}$ is obtained by: $S_{filter} = S_{raw}e^{-i\phi_{init}}$. Following, the first guesses of water and fat are calculated W_{init}, F_{init} .
3. The estimations $\phi_{init}, W_{init}, F_{init}$ are used to initialize the Gauss Newton algorithm, which outputs the final water-fat separation with the final fitted background phase W, F, ϕ .

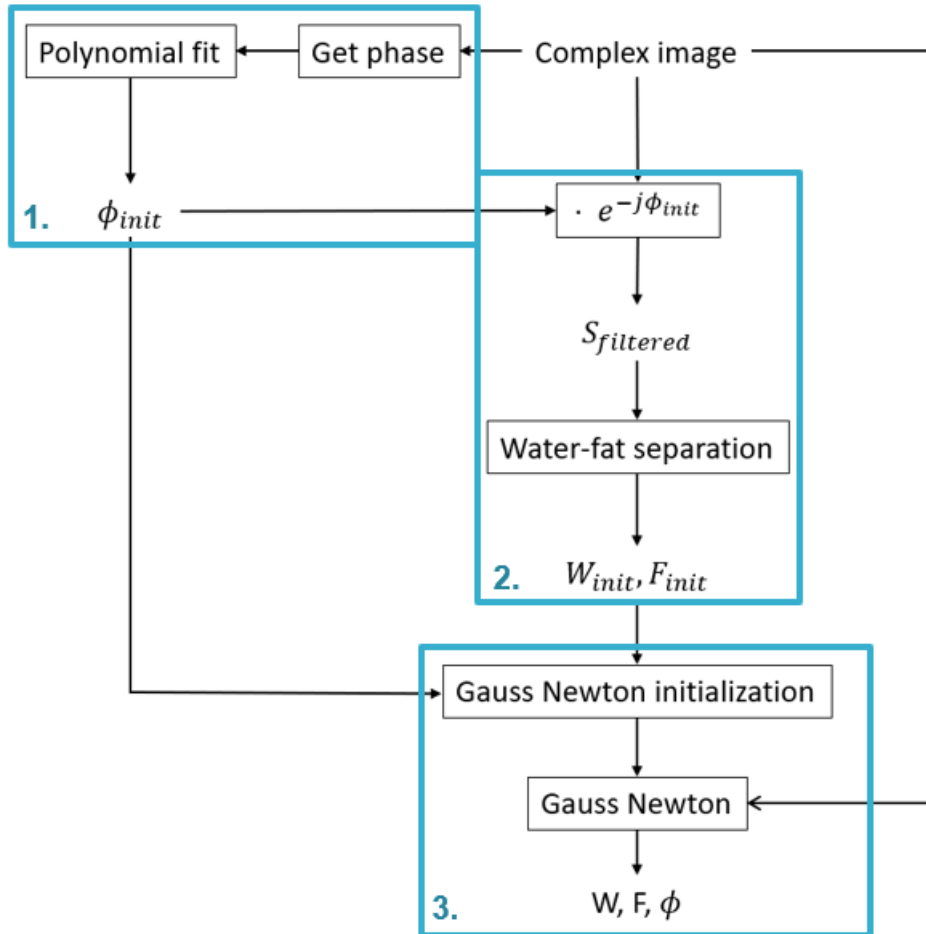


Figure 6.10: Gauss Newton Optimization with Initialization. The algorithm is divided in three main parts. 1. The signal UTE phase is unwrapped and taken as input of the polynomial fit. The output of this fit is the first guess of the background phase ϕ_{init} . 2. This background phase gets filtered out from the raw signal obtaining a filtered phase $S_{filtered}$ and from this the first guesses of the water and fat are calculated W_{init}, F_{init} . 3. The guesses $\phi_{init}, W_{init}, F_{init}$ are then input as initialization of the Gauss Newton optimization algorithm, from which we get the final water-fat separation with the final fitted background phase W, F, ϕ .

This algorithm is applied to the same set of clinical images as Krinthaler et al. [21]. There are three scanned anatomies: the cervical spine, the thoracic spine anterior and the lumbar spine. The 3D-UTE measurements were performed with a stack-of-stars center-out radial acquisition and phase-encoding in the third cartesian dimension on a clinical 3 T system (Elition X, Philips Healthcare). The scans were done with a sagittal orientation, a flip angle $\alpha = 5^\circ$ and a sense factor of $R = 1.5$. The specific parameters for the scans are found in Table 6.2.

Anatomy	Coil	FOV [mm ³]	Resolution [mm ³]	TE/TR [ms]	Scan time [min]	W/F-shift [px]
Thoracic Spine	Anterior Torso coil + posterior coil 32 channels	250x250x60	0.3x0.3x1.5	0.4/6.80	2 : 02 : 3	0.65454
Cervical Spine	Head/Neck coil 20 channels	220x220x60	0.3x0.3x1.5	0.4/6.63	1 : 45 : 0	0.65681
Lumbar Spine	Anterior Torso coil + posterior coil 32 channels	250x250x60	0.3x0.3x1.5	0.4/6.80	2 : 02 : 3	0.65454

Table 6.2: Measurement Parameters. For all the scans a sagittal orientation, a flip angle of 5° , and a SENSE factor of $R = 1.5$ was used.

The two variants of the Gauss Newton method with and without the polynomial fit initialization were compared in terms of water-fat separation results and the number of iteration till convergence at regularization factors of 1, 10 and 100. The convergence criteria was set to the relative phase update $\frac{\|d\phi_n\|}{\|\phi_n\|}$ being less than 0.01, or when the number of iterations of the Gauss Newton method exceeds a 100. [21]

6.2.2 Impact on ϕ^*

For the initial phase modeling we use a second order 3D polynomial $g = P_2$, as done for the phantom because of the inherent shape of the background B_1 phase ¹. The resulting ϕ_{init} is depicted in Figure 6.11, for different regularization parameters with their respective number of iterations till convergence. With increasing regularization, the resulting phase becomes smoother, resembling the plain polynomial fit solution. The number of iterations needed for convergence is displayed above each image. It is seen that the initialized algorithm offers a solid starting point, significantly reducing the iteration count for all regularization parameters. The other anatomies are shown in Section A.2

¹ To keep it brief, only the best found polynomial is used. The comparison with other initialization functions is done in Section A.1

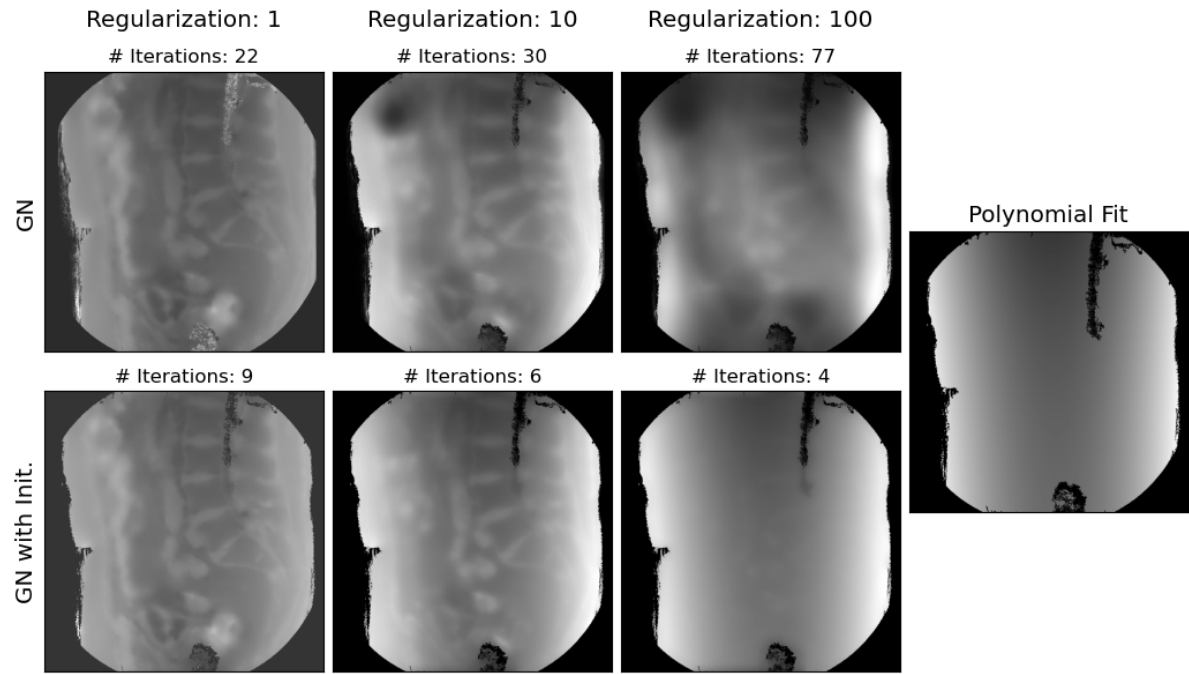


Figure 6.11: Resulting ϕ^* from the Gauss Newton (GN) and Gauss Newton with Initialization (GN with Init.) methods for the regularization parameters $\lambda = 1, 10, 100$. With increasing regularization the resulting phase is enforced to be smoother, approaching to the plain polynomial fit solution. The number of iterations till convergence are shown above every image. The initialized algorithm provides a good initialization, reducing the number of iterations substantially for every regularization parameter.

6.2.3 Impact on Water-Fat Separation

Water and fat images are separated from the different anatomies and the plain Gauss Newton (GN) method is compared to the initialized Gauss Newton (GN with Init.) method.

6.2.3.1 Cervical Spine

The results for the cervical spine are shown in [Figure 6.12](#). The water-fat separation quality is improved by the initialization having a better separation of the brain into water and fat. The spine and esophagus cavity are separated correctly for both cases.

A closeup on the regularization 100 is made in [Figure 6.13](#). The resulting separation of the brain and bone has a better quality in the initialized method. While some artifacts at the edges remain visible (indicated by green arrows),

other artifacts are reduced (indicated by red arrows), demonstrating an overall improvement in water-fat separation quality.

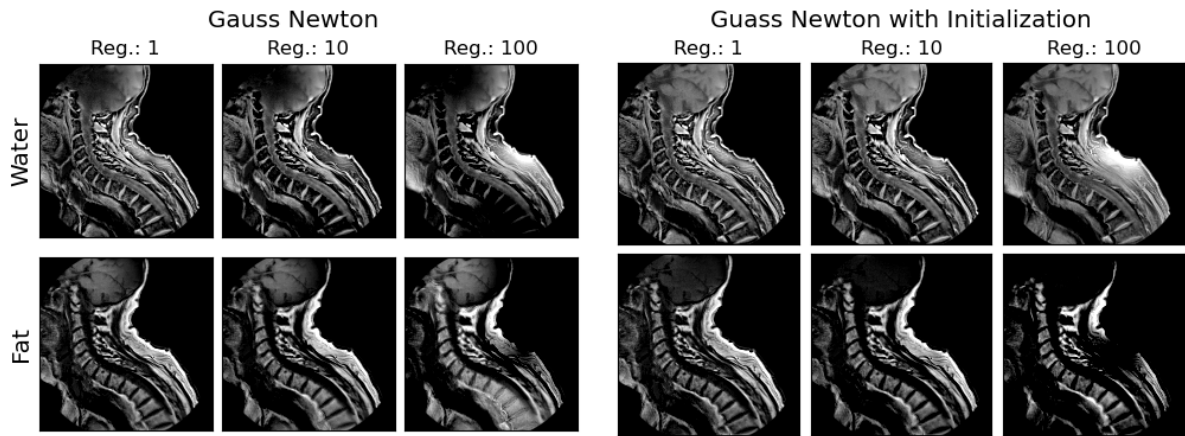


Figure 6.12: Resulting Water and Fat of the cervical spine from the Gauss Newton and Gauss Newton with Initialization methods for the regularization parameters $\lambda = 1, 10, 100$. The overall water-fat separation from the initialized algorithm delivers a better quality than the plain algorithm. Specially at the brain and bone.

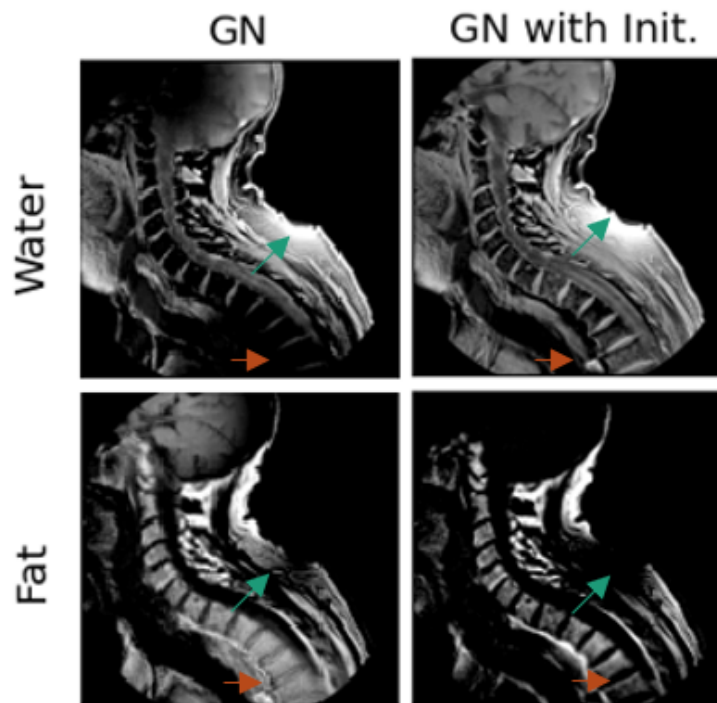


Figure 6.13: Resulting Water and Fat from the Gauss Newton (GN) and Gauss Newton with Initialization (GN with Init.) methods for regularization $\lambda = 100$. The water-fat separation of the brain and bone is superior in the initialized method. Although some artifacts at the edges are still seen (green arrows), also some artifacts are dimmed (red arrows), proving an overall better water-fat separation.

6.2.3.2 Thoracic Spine Anterior

For the next anatomy a more complex section is used. The thoracic spine is separated in the same manner into water and fat. As seen on [Figure 6.14](#), the water-fat separation quality deteriorates with higher regularization parameters, but in comparison to the non-initialized algorithm in this anatomy the initialization does not affect stability for the different regularization parameters. The heart, aorta and spine are well separated in the image.

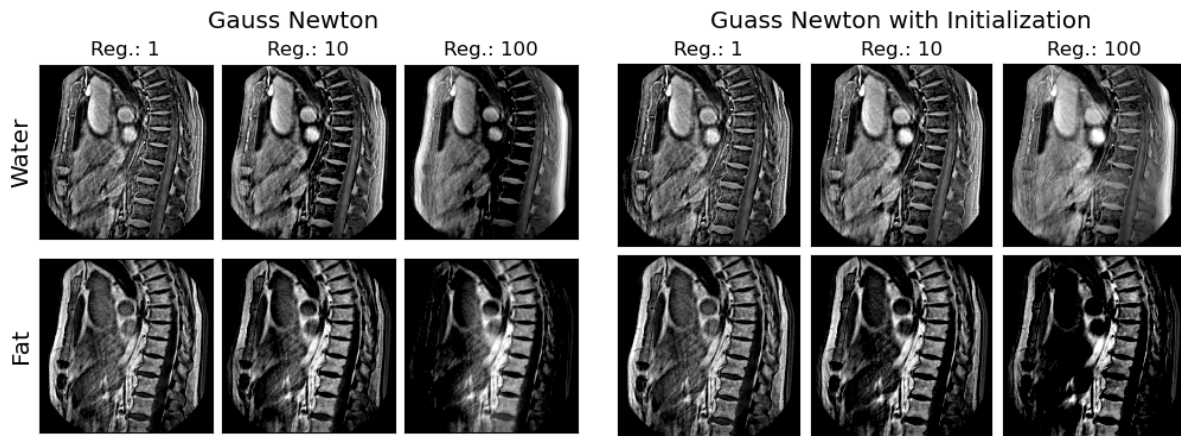


Figure 6.14: Resulting Water and Fat for the thoracic spine from the Gauss Newton and Gauss Newton with Initialization methods for the regularization parameters $\lambda = 1, 10, 100$. The water-fat separation is qualitatively the same for both cases. No stability is lost with increasing regularization.

To highlight the impact of the initialization in the water-fat separation in the thoracic spine. A zoom is made in the fat separation for $\lambda = 100$ in [Figure 6.15](#). The resulting fat separation is similar for both cases. although, the fat separation for the skin fat at the edges seems improved by the initialization (indicated by green arrows), and other streaking artifacts, in the difficult to separate inner abdomen, are reduced (indicated by red arrows).

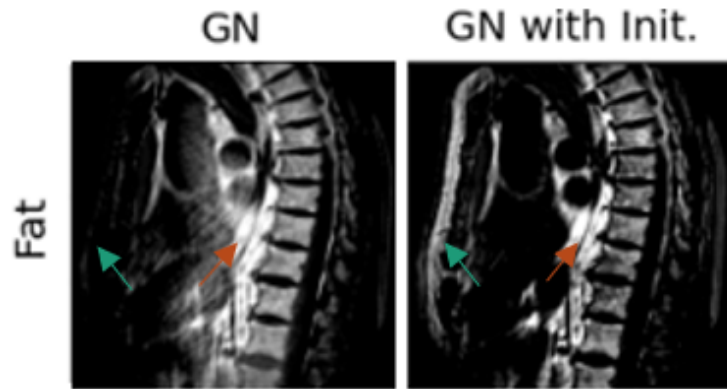


Figure 6.15: Resulting fat from the Gauss Newton (GN) and Gauss Newton with Initialization (GN with Init.) methods for regularization $\lambda = 100$. Separation delivers roughly the same quality on both methods. Although the separation of the skin fat is improved by the initialization (green arrows), and some streaking artifacts in the inner abdomen are dimmed (red arrows).

6.2.3.3 Lumbar Spine

Going further down the thorax the lumbar spine is separated into water and fat using both methods. Depicted on Figure 6.16 can be seen that the water-fat separation quality deteriorates with higher regularization parameters for the non-initialized method, only delivering good results for low-medium regularization parameters. The initialized method offers an advantage in comparison to its counterpart, delivering better water-fat separation for higher regularization.

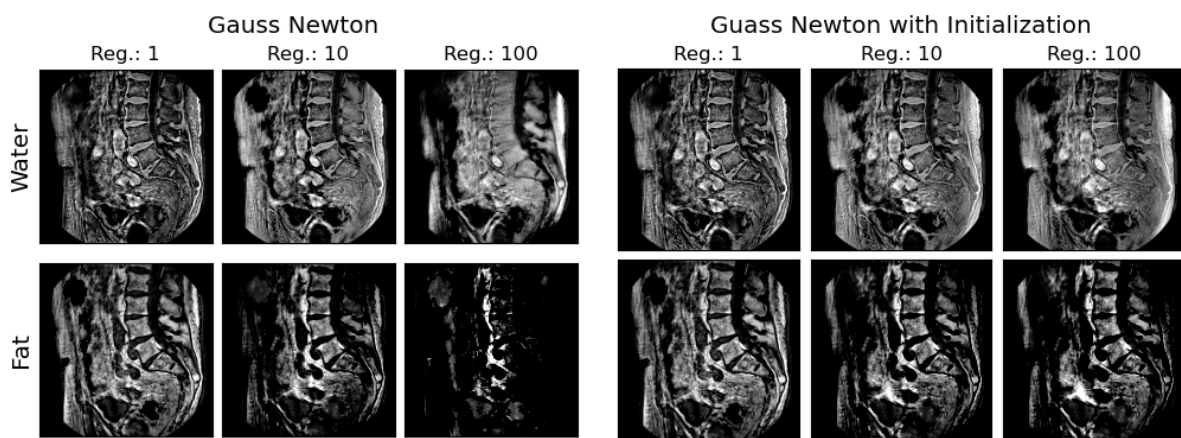
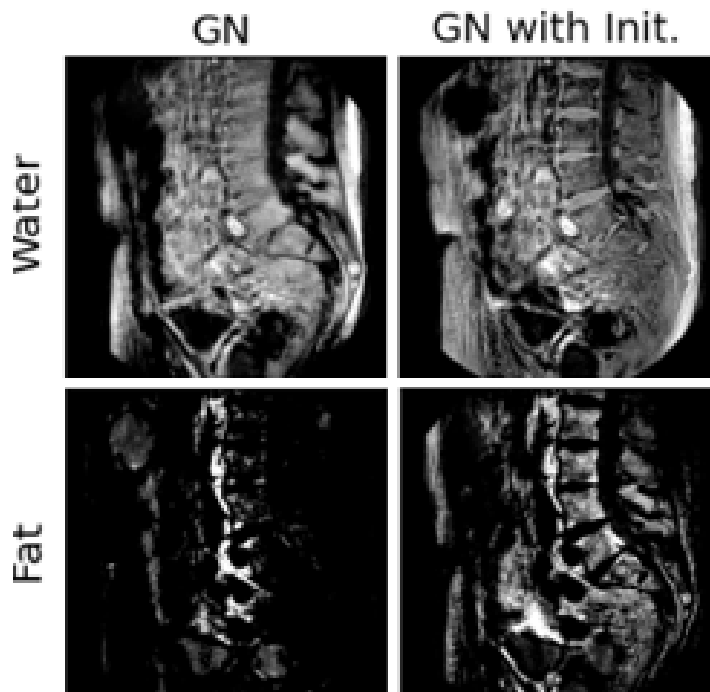


Figure 6.16: Resulting Water and Fat for the lumbar spine from the Gauss Newton and Gauss Newton with Initialization methods for the regularization parameters $\lambda = 1, 10, 100$. The water-fat separation is qualitatively the same for small regularization. But stability is rapidly lost with increasing regularization for the non-initialized method, while its counterpart remains robust.

The impact of the initialization of the method is emphasized by zooming in the water-fat separation for $\lambda = 100$ in [Figure 6.17](#). The non-initialized algorithm stops delivering good results, affecting the separation of the spine and skin fat completely. While the initialized algorithm depicts the spine and skin fat batter at higher regularization parameters.



[Figure 6.17](#): Resulting fat from the Gauss Newton (GN) and Gauss Newton with Initialization (GN with Init.) methods for regularization $\lambda = 100$. There is a substantial difference between the water fat separation of the non-initialized versus the initialized method. The initialized method delivers a fairly correct water-fat separation. Whereas the non-initialized method stops delivering a good separation quality for regularization $\lambda = 100$

From the resulting images it is studied how initialization impacts the resulting phase, water and fat of the method. The common trend shows that with increasing regularization there is loss of stability in the water-fat separation. This results are discussed in [Chapter 7](#).

B_0 MODELING AS A PRE-INITIALIZATION

6.3 B_0 MODELING AS A PRE-INITIALIZATION

Having tested the effects of initialization in the Gauss Newton algorithm. The, till now, neglected term B_0 is studied. For this, the signal is pre-filtered by the modeled B_0 phase contribution given by [6.1](#), which we call *forward model*. The resulting phase ϕ_{B_0} is then filtered from the signal and then input into the Gauss Newton with Initialization algorithm [Algorithm 2](#). The algorithm is described in [Algorithm 3](#), where the air chi-map $\hat{\chi}$ is masked with a shift of 9.2 ± 1.3 ppm [4] from the center frequency, and the tissue $\hat{\chi}$ is set to 0.

Algorithm 3 B_0 pre-initialization

```
1:  $UTEphase \leftarrow \text{Unwrap}(\angle(S_{raw}))$ 
2:  $M \leftarrow \text{getFilledAnamotyMask}(UTEphase)$ 
3: if isLung(Anatomy) then
4:    $M_{Lung,Air} \leftarrow \text{getLungAirMask}(S_{raw})$ 
5:    $\hat{\chi} \leftarrow M_{Lung,Air} * 9.2$ 
6: end if
7:  $\phi_{B_0} \leftarrow \text{Equation 6.1 } (\hat{\chi})$ 
8:  $S_0 \leftarrow S_{Raw} e^{-i\phi_{B_0}}$ 
9:  $\phi^*, W^*, F^* \leftarrow \text{Gaussian Optimization with Initialization}(\lambda, S_0, *args)$ 
10: return  $\phi^*, W^*, F^*$ 
```

The method is tested specifically for difficult organs such as lungs, because this big organ filled with air introduces important field inhomogeneities in its borders with other tissues.

6.3.1 Validation

First we validate the generated water-fat of the method added the pre-initialization forward model, with the results in [Section 6.2](#). The three anatomies are depicted in [Figures 6.18, 6.19 and 6.20](#). The results of the method with forward model are virtually equal to the plain method separa-

tions. Thus, the forward model is valid and do not disturb the results for these anatomies.

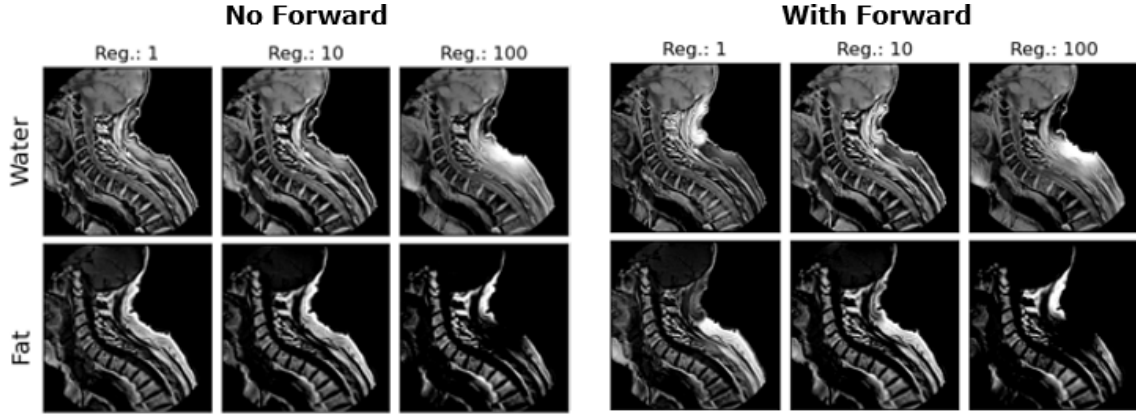


Figure 6.18: Resulting Water and Fat of the cervical spine from the forward modeled and plain initialized Gauss Newton methods for the regularization parameters $\lambda = 1, 10, 100$. The results have virtually the same quality.

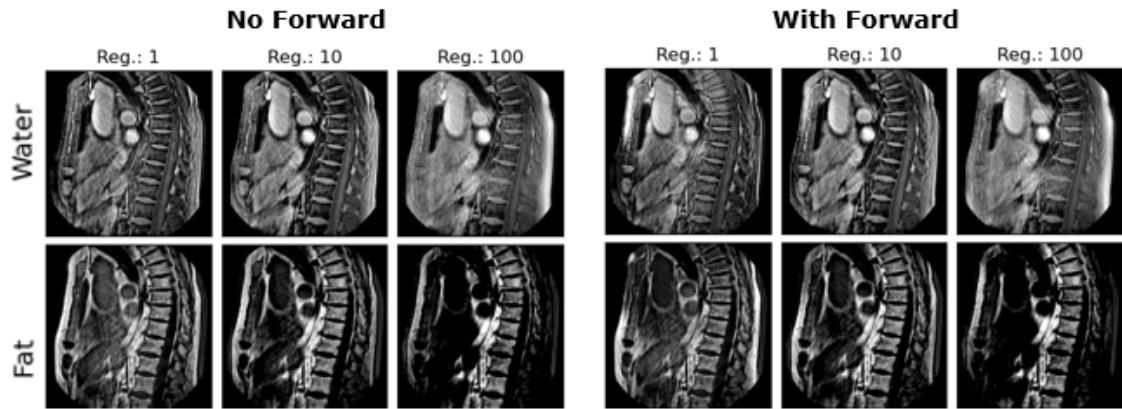


Figure 6.19: Resulting Water and Fat of the thoracic spine from the forward modeled and plain initialized Gauss Newton methods for the regularization parameters $\lambda = 1, 10, 100$. The results have virtually the same quality.

6.3.2 Water-Fat Separation in the Lung

Two lung images are separated into water and fat by the forward-modeled and plain initialized Gauss Newton method and both results are compared. For this the lungs are masked and the forward model is done using this mask. An example of a B_0 modeled phase of the lung is depicted in [Figure 6.21](#), where the used mask is implicitly seen, note how the structures inside the lung are not masked since they are different than air, hence, the different phase.

The results are depicted in [Figures 6.22 and 6.23](#). In both cases the separation is similar for high regularization, but in low regularization both cases deliver better results when B_0 is not filtered before the method. In the second scan [Figure 6.23](#), the non-forward modeled method works better even in medium regularization $\lambda = 10$.

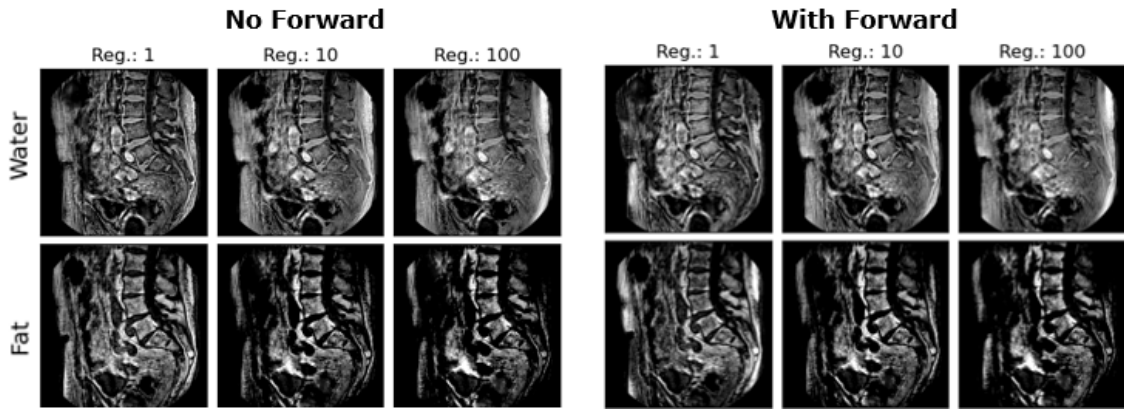


Figure 6.20: Resulting Water and Fat of the lumbar spine from the forward modeled and plain initialized Gauss Newton methods for the regularization parameters $\lambda = 1, 10, 100$. The results have virtually the same quality.

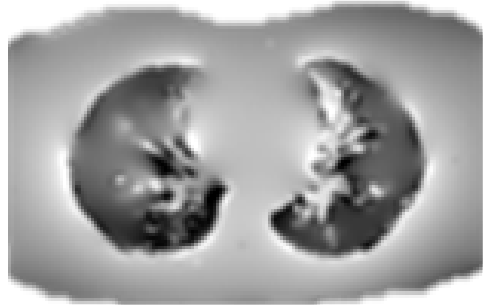


Figure 6.21: Resulting B_0 induced phase map for a lung scan. The used lung mask is implicitly seen from the different phase inside the lungs.

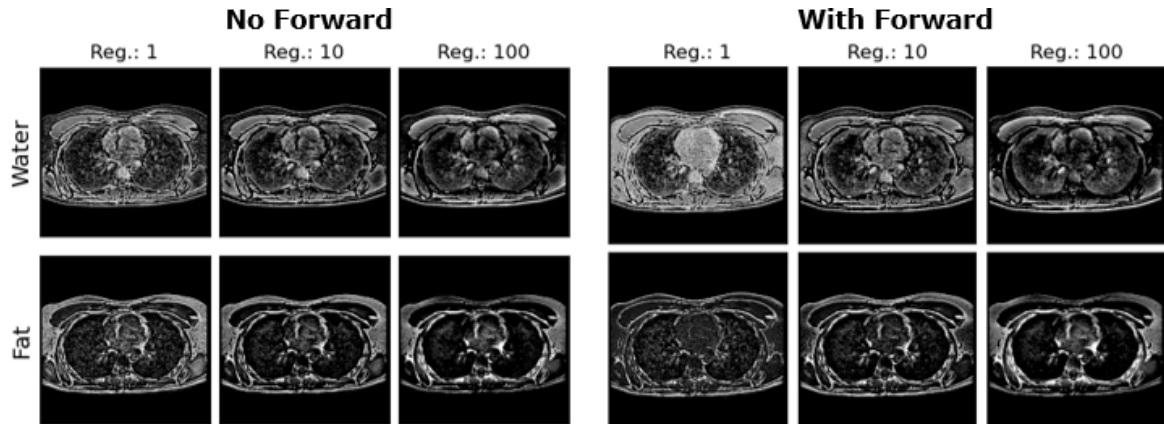


Figure 6.22: Resulting Water and Fat of the lung from the forward/no-forward modeled methods for the regularization parameters $\lambda = 1, 10, 100$. The results for the forward/no forward modeling are similar for medium-high regularization. But for low regularization $\lambda = 1$ the separation is better without the B_0 pre-initialization.

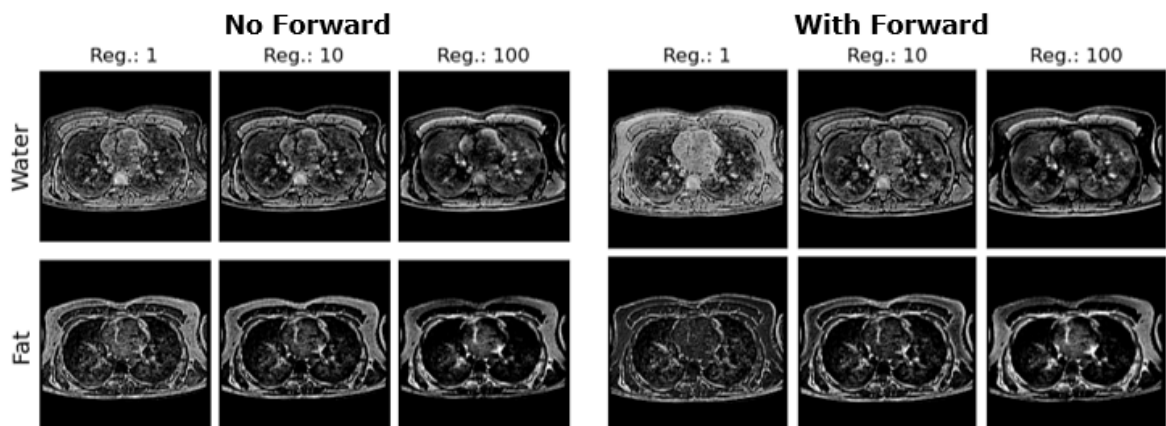


Figure 6.23: Resulting Water and Fat of the lung from the forward/no-forward modeled methods for the regularization parameters $\lambda = 1, 10, 100$. The results for the forward/no forward modeling are only similar for high regularization. But for low and medium regularization $\lambda = 1, 10$ the separation is better without the B_0 pre-initialization.

DISCUSSION AND CONCLUSION

After an extensive analysis, the results presented in [Chapters 6, 6.2 and 6.3](#) are summarized and interpreted. The implications of such findings are explained as well as its limitations.

DISCUSSION

7.1 PHASE CONTRIBUTIONS

In this section we focus on the results from [Chapter 6](#).

From [Figure 6.2](#), the higher induced conductivity because of the added salt affects the shape of the inner water phase, even making it appear as an *upwards bowl* shape as seen in [Figure 6.5](#), where its contour resembles the sum of spherical harmonics as discussed in theory for B_1 , spherical harmonics are just polynomials with special properties. Hence, its formula may be approximated by polynomials with the correct parameters a_i . A second-degree 3D polynomial was chosen to model this contributions.

The B_0 contributions are small compared to B_1 contributions, as promptly seen in [Figure 6.3](#) with short values. This has to do with the little accumulation of phase because of the really small echo times in UTE. Also, the modeling and filtering of the B_1 phase contribution is much more relevant than the B_0 visualized in [Figure 6.4](#), since it helps substantially to flatten the phase visually. This is further validated in the line-plots of the phases [Figure 6.9](#) where it is clear how the B_0 phase cannot capture the curvature of the UTE-phase. Whereas, the B_1 phase has an inherent curvature and thus can be fit to a curved phase.

Finally, a conclusive measurement is made by calculating the *flatness* of the image after the respective phase modeling and filtering. The measure used is the sum of gradients and the regions were also masked to have a relevant result. From the results in [Table 6.1](#), it is shown how B_1 phase modeling and filtering is so much relevant to the final flatness of the phase and hence its more important to the background bulk phase contributions ψ_{bulk} . Its difference between the flatness of the B_0 & B_1 filtered phases are of orders of magnitude, highlighting further the importance of choosing to model B_1 over B_0 .

7.2 INITIALIZATION IMPACT ON WATER-FAT SEPARATION

We focus on the results presented in [Section 6.2](#) and its implications.

The choice of using a second degree 3D polynomial is not only because it was a good fit for the phantom (See [Figure 6.5](#)). But multiple initialization functions were conducted. Nevertheless, the best results were delivered from the second degree 3D polynomial for further reading the tests are in [Section A.1](#).

7.2.1 *Impact on ϕ^**

The impact of the initialization on ϕ^* is analyzed in [Section 6.2.2](#).

Taking a look to [Figure 6.11](#), it is emphasized how with increasing regularization both the plain and the initialized method approach to the result of the direct polynomial fit to the UTE phase. In this case, initialization makes the phase smoother and also eliminates some unwanted dark patches as seen in the image. Moreover, the number of iterations till convergence are also strongly reduced, specially for high regularization.

These results hint to an improved convergence path, since a smoother fit for ϕ^* in conjunction to a reduction of the number of steps required till convergence, implies that the starting point ϕ_{init} coming from the initialization method, directs the algorithm in the right direction.

To further prove the latter point, we take a look into the water-fat separation results for different regularization parameters on multiple anatomies.

7.2.2 *Effects on Water-Fat separation*

The effects of initialization on water-fat separation is studied in [Section 7.2](#).

Cervical Spine

The cervical spine is first analyzed. From [Figure 6.12](#) it is clearly seen how the brain separation is improved by the initialization of the method. In the plain Gauss Newton method the brain is separated as a mix of both water and fat. As is known from the theory brain is mostly water, which is a contradiction from this separation. This is not the case for the initialized algorithm, since brain and bone are both correctly separated.

Doing a zoom-in on the separation with $\lambda = 100$ the differences are annotated by **red** and **green** arrows, see [Figure 6.13](#). The bone is correctly separated in both cases, although in the initialized method the artifacts are dimmed and the separation at the scan's edges is improved, as indicated by the **red** arrows. But some artifacts still remain on the image, proving that initialization has its limitations at the tissue-air edges, as seen by the **green** arrows.

We note that the water fat separation for this anatomy delivers its best results with a mid regularization $\lambda = 10$. When $\lambda = 1$ the brain is not depicted correctly in any of the methods, and using $\lambda = 100$ introduces edge artifacts.

Thoracic Spine

Next, the thoracic spine is studied. Having multiple moving organs and specially lungs and heart, the thoracic spine proves to be a harder anatomy to separate. The results are seen in [Figure 6.14](#). On both methods the heart and its main vessels, as well as the bone are correctly separated, and not only the big structures but also the fine ones, such as the fatty tissue covering the heart and its vessels, are also correctly separated. The results are very similar.

As for the cervical spine, we highlight that with $\lambda = 100$ issues start to appear in both methods. For this anatomy, the separation of the inner thorax starts to become unstable, and also high phase peaks at the back of the anatomy start to appear.

A close-up is made on the thoracic spine fro $\lambda = 100$, see [Figure 6.15](#) and the differences between both methods are highlighted by **red** and **green** arrows. The **red** arrow shows how the streaking effects, presumably coming from the lung, are reduced in the initialized method in the inner abdomen. Similarly, the **green** arrows point to the superficial fat layer of the skin, which is corrupted from the high regularization for the plain method, but slightly corrected for the initialized method.

Lumbar Spine

Finally, the lumbar spine is analyzed. The separation is seen in [Figure 6.16](#). On this anatomy the effects of increasing regularization are the most noticeable. For low λ the bone is separated correctly on both methods, but with higher regularization, the quality of the water-fat separation decreases on both methods. Most importantly, the water-fat separation becomes invalid on the plain method with high regularization.

zooming-in in [Figure 6.17](#) the impact of initialization with a regularization of $\lambda = 100$ for this anatomy is clear. The fat separation of the plain method is opaque and no discernible structures can be seen in the image. For the lumbar spine, initialization adds robustness to the method, making it viable even for high regularization.

7.3 IMPACT OF B_0 MODELING

The results on the effects of the adding *forward modeling* filtering before the method are presented in [Section 6.3](#).

7.3.1 Validation

As seen from the validation step in [Figures 6.18, 6.19 and 6.20](#), modeling B_0 and filtering out from the signal before processing does not visually affect the results where no lung is modeled, but it does not improve the quality of the separation either. Since the effect of B_0 on the signal is much lower than that from B_1 is to be expected, because the only modeled air in the anatomies is the one outside the anatomy (black background).

7.3.2 Impact on Lung scans

The resulting B_0 phase map for one of the lung scans is depicted in [Figure 6.21](#). It is illustrated how the mask captures the lung. It is also seen how the bronchi are modeled despite being inside the lung introducing more complexity to the forward modeled phase.

Following, the initialized method with and without forward modeling is compared. There is no distinguishable improvement for the use of the B_0 filtering in the context of the initialized Gauss Newton method. It is expected, since the flexibility of the iterative optimization enables the fit to capture this low magnitude and low varying phase, despite not taking it into account in the initialization.

As with the results discussed in [Section 7.2](#), the water-fat separation stability decreases at high regularization parameters. For the forward modeled results even at low $\lambda = 1$ the quality of the water-fat separation is decreased. More-

over, a slightly better separation is done by the non-forward modeled method for $\lambda = 10$ than its counterpart.

7.4 LIMITATIONS

By testing on the phantom and the different anatomies, the weaknesses of the initialization and the modeling of the field inhomogeneities phase contributions were identified. Here, we mention the most important limitations and give some ideas for improvement.

Limitations in Modeling Phase Contributions

In general, it is demonstrated that the B_1 field contributions to the bulk phase is much more relevant than the main field B_0 contributions. Nevertheless, the complexity of a multiple tissue anatomy is much higher and cannot be modeled perfectly by a plain polynomial for the whole image. This can limit the quality of the inference that we can do from the given results for the phantom in more complex anatomies.

If we follow Maxwell's equations the solution relies on doing this fit for every different tissue separately and account for the tissue edges in some manner. This is computationally complex and costly. Reason why it could only be done for the phantom, but not for the clinical anatomies such as the thoracic and cervical spine, which include various tissues with different artifacts, motions and electrical properties. Still, since the difference of this effects in the UTE scans are in the orders of magnitude (as seen in [Section 7.1](#)), we can proceed with the results that B_1 is a more important contribution to UTE scans than B_0 .

Limitations of Initialization

It is clearly shown that initialization has a positive impact on the otherwise zero-initialized Gauss Newton iterative optimization method, both on the water-fat separation quality as well reducing the number of iterations needed for convergence, and robustness of the model. However, initialization has its limitations:

- **Modeling of the phase contributions:** As discussed above, if there is no perfect B_1 modeling there cannot be a perfect initialization either. Improving B_1 modeling techniques is required to further enhance the method.

- **Ill-posedness:** Although initialization could be *perfect*, the kernel of the optimization problem has infinite solutions. Hence, one can never guarantee that the given result can be trusted blindly. Developing newer, well-defined techniques with a proper solution space is needed to quantify the resulting water-fat separation for single-point UTE, instead of only having qualitative relevant results.
- **Sensitivity to the regularization parameter λ :** Albeit the increased robustness with respect to λ , there is still some sensitivity and a clear trend with this hyper-parameter. With increasing regularization the results become poorer. Hence, a proper choice for λ is still needed for an optimal water-fat separation.

Limitations of Forward Modeling

As discussed in [Section 7.3](#) there is no improvement seen for the B_0 modeling and pre-filtering method. Its limitations arise from the iterative optimization, which is flexible enough to fit also the underlying B_0 phase from the scan during processing. This causes the pre-filtered method to be *over-fitted* since the B_0 background phase is fit twice. Decreasing the separation quality.

7.5 IMPLICATIONS

The importance of initializing the ill-posed method is highlighted during the study. It is shown that simple initialization techniques improve the convergence path of the optimization method. It is also demonstrated that the B_1 field inhomogeneities are the main driver of the background phase in UTE, which can be used by other novel-techniques to further improve them by endorsing the importance of modeling such phase contributions. Finally, it is remarked that the B_0 modeling and filtering form the raw signal is not needed, and even, in some cases detrimental to the performance of the initialized Gauss Newton optimization method. This, because the iterative method already has the flexibility to model such changes and thus, can be over-fitted when setting the starting point with an already filtered signal.

CONCLUSION

This work investigated the problem of background phase modeling and initialization of the novel ill-posed iterative optimization method presented by Kronthaler et. al. [21].

The results of this study demonstrate that the single-point UTE Dixon imaging technique effectively separates water and fat signals, even in the presence of B_0 and B_1 field inhomogeneities. Our findings are consistent with and, in some instances, improve upon those reported by Kronthaler et al. [21], highlighting the efficacy of an iterative optimization method for water-fat separation.

One of the significant implications of our study is the potential for faster MRI scans without compromising image separation quality. By reducing the number of required iterations, the initialized algorithm enhances computational efficiency, potentially leading to shorter post-processing times in clinical settings. However, some artifacts persist at the edges of the images, indicating the need for further refinement of the phase modeling and initialization processes.

Despite the overall success, our study has certain limitations. The sample size was relatively small, and the phantoms used may not fully replicate the complexity of human tissues. Future research should focus on testing the algorithm with a larger, more diverse sample and exploring additional initialization techniques to further minimize artifacts.

Furthermore, our investigation underscores the importance of initializing the ill-posed method to improve the convergence path of the optimization method. It is evident that B_1 field inhomogeneities are the primary contributors to the background phase in UTE, suggesting that novel techniques should prioritize modeling these phase contributions for enhanced performance. Conversely, B_0 modeling and filtering from the raw signal appear unnecessary and, in some cases, detrimental to the performance of the initialized Gauss-Newton optimization method due to potential over-fitting.

The presented single-point UTE Dixon imaging technique offers a promising approach for effective water-fat separation, with significant implications for improving the efficiency and accuracy of water-fat separation post-processing for MRI scans. Future research efforts should aim to address the identified limitations, modeling the phases in a more complex manner as well as further refine the initialization methodology to ensure its robustness and applicability in diverse clinical scenarios.

Finally, this research has demonstrated that the single-point UTE Dixon imaging technique, enhanced with an initialization algorithm, can achieve effective water-fat separation with improved computational efficiency and robustness with respect to the regularization parameter λ . These findings contribute to the ongoing efforts to optimize MRI techniques, potentially leading to faster and more accurate diagnostic imaging.

BIBLIOGRAPHY

- [1] In *Wikipedia*. 2024. URL: https://en.wikipedia.org/wiki/Magnetic_resonance_imaging.
- [2] Ferruccio Balestra et al. “ \bar{p}^4 He reaction cross section at 610 MeV/c.” In: ().
- [3] T. Baum, C. Cordes, M. Dieckmeyer, S. Ruschke, D. Franz, H. Hauner, J. S. Kirschke, and D. C. Karampinos. “MR-based assessment of body fat distribution and characteristics.” In: *European Journal of Radiology* 85.8 (2016), pp. 1512–1518.
- [4] Sagar Buch, Saifeng Liu, Yongquan Ye, Yu-Chung Norman Cheng, Jaladhar Neelavalli, and E. Mark Haacke. “Susceptibility mapping of air, bone, and calcium in the head.” In: *Magnetic Resonance in Medicine* 73.6 (2015), pp. 2185–2194. DOI: <https://doi.org/10.1002/mrm.25350>.
- [5] Adrienne Campbell-Washburn. “MRI: The Classical Description.” In: *Proceedings of the 26th Annual Meeting of the International Society for Magnetic Resonance in Medicine (ISMRM)*. Paris, France, 2018. URL: <https://cds.ismrm.org/protected/18MProceedings/PDFfiles/E1030.html>.
- [6] B. D. Coombs, J. Szumowski, and W. Coshow. “Two-point Dixon technique for water-fat signal decomposition with Bo inhomogeneity correction.” In: *Magnetic Resonance in Medicine* 38.6 (Dec. 1997), pp. 884–889. DOI: [10.1002/mrm.1910380606](https://doi.org/10.1002/mrm.1910380606).
- [7] M. N. Diefenbach, S. Ruschke, H. Eggers, J. Meineke, E. J. Rummeny, and D. C. Karampinos. “Improving chemical shift encoding-based water-fat separation based on a detailed consideration of magnetic field contributions.” In: *Magnetic Resonance in Medicine* 80.3 (2018), pp. 990–1004. ISSN: 0740-3194.
- [8] W. T. Dixon. “Simple proton spectroscopic imaging.” In: *Radiology* 153.1 (Oct. 1984), pp. 189–194. DOI: [10.1148/radiology.153.1.6089263](https://doi.org/10.1148/radiology.153.1.6089263).

- [9] D. Franz, J. Syväri, D. Weidlich, T. Baum, E. J. Rummeny, and D. C. Karampinos. “Magnetic Resonance Imaging of Adipose Tissue in Metabolic Dysfunction.” In: *RöFo-Fortschritte auf dem Gebiet der Röntgenstrahlen und der bildgebenden Verfahren* 190.12 (2018), pp. 1121–1130.
- [10] H. M. Gach, A. N. Curcuru, S. Mutic, and T. Kim. “Bo field homogeneity recommendations, specifications, and measurement units for MRI in radiation therapy.” In: *Medical Physics* 47.9 (Sept. 2020). Epub 2020 Jul 19, pp. 4101–4114. DOI: [10.1002/mp.14306](https://doi.org/10.1002/mp.14306).
- [11] G. H. Glover and E. Schneider. “Three-point Dixon technique for true water/fat decomposition with Bo inhomogeneity correction.” In: *Magnetic Resonance in Medicine* 18.2 (Apr. 1991), pp. 371–383. DOI: [10.1002/mrm.1910180211](https://doi.org/10.1002/mrm.1910180211).
- [12] Vikas Gulani and Nicole Seiberlich. “Quantitative MRI: Rationale and Challenges.” In: *Quantitative Magnetic Resonance Imaging*. Ed. by Nicole Seiberlich, Vikas Gulani, Fernando Calamante, Adrienne Campbell-Washburn, Mariya Doneva, Houchun Harry Hu, and Steven Sourbron. Vol. 1. Advances in Magnetic Resonance Technology and Applications. Academic Press, 2020, pp. xxxvii–li.
- [13] E. M. Haacke, R. W. Brown, M. R. Thompson, and R. Venkatesan. *Magnetic Resonance Imaging: Physical Principles and Sequence Design*. Vol. 82. New York: Wiley-Liss, 1999.
- [14] L. G. Hanson. “Is quantum mechanics necessary for understanding magnetic resonance?” In: *Concepts in Magnetic Resonance Part A* 32A.5 (2008), pp. 329–340.
- [15] R. M. Henkelman, G. J. Stanisz, and G. J. Graham. “Magnetization transfer in MRI: a review.” In: *NMR in Biomedicine* 14 (2001), pp. 57–64.
- [16] D. Hernando, P. Kellman, J. P. Haldar, and Z. P. Liang. “Robust water/-fat separation in the presence of large field inhomogeneities using a graph cut algorithm.” In: *Magnetic Resonance in Medicine* 63.1 (Jan. 2010), pp. 79–90. DOI: [10.1002/mrm.22177](https://doi.org/10.1002/mrm.22177).
- [17] Hyungseok Jang, Michael Carl, Yajun Ma, Saeed Jerban, Tan Guo, Wei Zhao, Eric Y. Chang, and Jiang Du. “Fat suppression for ultrashort echo time imaging using a single-point Dixon method.” In: *NMR in Biomedicine* 32.5 (2019). e4069 NBM-18-0167.R3, e4069. DOI: <https://doi.org/10.1002/nbm.4069>.

- [18] U. Katscher and C. A. T. van den Berg. “Electric properties tomography: biochemical, physical and technical background, evaluation and clinical applications.” In: *NMR in Biomedicine* 30.8 (2017), nbm.3729. DOI: [10.1002/nbm.3729](https://doi.org/10.1002/nbm.3729).
- [19] James Keeler. *Spin Dynamics: Basics of Nuclear Magnetic Resonance*. 2nd. Wiley, 2005. ISBN: 9780470511176. URL: <https://www.wiley.com/>.
- [20] D. H. Kim, N. Choi, S. M. Gho, J. Shin, and C. Liu. “Simultaneous imaging of in vivo conductivity and susceptibility.” In: *Magnetic Resonance in Medicine* 71.3 (2014), pp. 1144–1150. DOI: [10.1002/mrm.24784](https://doi.org/10.1002/mrm.24784).
- [21] Sophia Kronthalter, Christof Boehm, Georg Feuerriegel, Peter Börnert, Ulrich Katscher, Kilian Weiss, Marcus R. Makowski, Benedikt J. Schwaiger, Alexandra S. Gersing, and Dimitrios C. Karampinos. “Assessment of vertebral fractures and edema of the thoracolumbar spine based on water-fat and susceptibility-weighted images derived from a single ultra-short echo time scan.” In: *Magnetic Resonance in Medicine* 87.4 (2022), pp. 1771–1783. DOI: <https://doi.org/10.1002/mrm.29078>. eprint: <https://onlinelibrary.wiley.com/doi/pdf/10.1002/mrm.29078>. URL: <https://onlinelibrary.wiley.com/doi/abs/10.1002/mrm.29078>.
- [22] Sophia Kronthalter, Georg Feuerriegel, Philipp Braun, Kilian Weiss, Alexandra Gersing, and Dimitrios C. Karampinos. “UTE–Dixon Fat–Water Imaging.” In: *MRI of Short- and Ultrashort-T₂ Tissues: Making the Invisible Visible*. Ed. by Jiang Du and Graeme M. Bydder. Cham: Springer International Publishing, 2023, pp. 191–201. ISBN: 978-3-031-35197-6. DOI: [10.1007/978-3-031-35197-6_15](https://doi.org/10.1007/978-3-031-35197-6_15). URL: https://doi.org/10.1007/978-3-031-35197-6_15.
- [23] Z.-P. Liang and P. C. Lauterbur. *Principles of Magnetic Resonance Imaging: A Signal Processing Perspective*. SPIE Optical Engineering Press, 2000.
- [24] A. L. van Lier, D. O. Brunner, K. P. Pruessmann, D. W. Klomp, P. R. Luijten, J. J. Lagendijk, and C. A. van den Berg. “B₁(+) phase mapping at 7 T and its application for in vivo electrical conductivity mapping.” In: *Magnetic Resonance in Medicine* 67.2 (2012), pp. 552–561. DOI: [10.1002/mrm.23025](https://doi.org/10.1002/mrm.23025).

- [25] Mohammad Mansouri, Shima Aran, Harlan B. Harvey, Khalid W. Shaqdan, and Hani H. Abujudeh. “Rates of safety incident reporting in MRI in a large academic medical center.” In: *Journal of Magnetic Resonance Imaging* 43.4 (2016), pp. 998–1007.
- [26] W. McFarlane. “A ^{13}C and ^{31}P magnetic double resonance study of organo-phosphorus compounds.” In: *Proceedings of the Royal Society of London. Series A, Mathematical and Physical Sciences*. Vol. 306. 1968, pp. 185–199.
- [27] Kay Nehrke and Peter Börnert. “DREAM—a novel approach for robust, ultrafast, multislice B_1 mapping.” In: *Magnetic Resonance in Medicine* 68.5 (2012), pp. 1517–1526. doi: <https://doi.org/10.1002/mrm.24158>.
- [28] S. Nielles-Vallespin, P. Speier, S. Komatsu, et al. “Atherosclerotic Plaque Imaging with Ultra Short Echo Time (UTE) MRI.” In: *Proceedings of the 15th Annual Meeting of ISMRM*. Abstract 440. 2007.
- [29] Radiology Cafe. *Radiology Cafe - FRCR Physics Notes: MR Imaging - Gradient-Recalled Echo Sequence*. Accessed: 2024, May 20. URL: <https://www.radiologycafe.com/>.
- [30] John Ridgway. “Cardiovascular magnetic resonance physics for clinicians: Part I.” In: *Journal of cardiovascular magnetic resonance : official journal of the Society for Cardiovascular Magnetic Resonance* 12 (Nov. 2010), p. 71. doi: [10.1186/1532-429X-12-71](https://doi.org/10.1186/1532-429X-12-71).
- [31] Matthew D. Robson, Peter D. Gatehouse, Mark Bydder, and Graeme M. Bydder. “Magnetic Resonance: An Introduction to Ultrashort TE (UTE) Imaging.” In: *Journal of Computer Assisted Tomography* 27.6 (Nov. 2003), pp. 825–846.
- [32] Karin Shmueli, Jacco A de Zwart, Peter van Gelderen, Tie-Qiang Li, Tie-Qiang Li, Stephen J Dodd, and Jeff H Duyn. “Magnetic susceptibility mapping of brain tissue *in vivo* using MRI phase data.” In: *Magnetic resonance in medicine* 62.6 (Dec. 2009), pp. 1510–1522. ISSN: 0740-3194. doi: [10.1002/mrm.22135](https://doi.org/10.1002/mrm.22135). URL: <https://europepmc.org/articles/PMC4275127>.
- [33] T. E. Skinner and G. H. Glover. “An extended two-point Dixon algorithm for calculating separate water, fat, and Bo images.” In: *Magnetic Resonance in Medicine* 37.4 (Apr. 1997), pp. 628–630. doi: [10.1002/mrm.1910370426](https://doi.org/10.1002/mrm.1910370426).

- [34] S. M.-H. Song, S. Napel, N. J. Pelc, and G. H. Glover. “Phase unwrapping of MR phase images using Poisson equation.” In: *IEEE Transactions on Image Processing* 4.5 (1995), pp. 667–676. ISSN: 1057-7149.
- [35] Philips Medical Systems. *Basic Principles of MR Imaging*. Eindhoven, Netherlands: Philips Medical Systems, 1984.
- [36] J. Szumowski, W. R. Coshow, F. Li, and S. F. Quinn. “Phase unwrapping in the three-point Dixon method for fat suppression MR imaging.” In: *Radiology* 192.2 (Aug. 1994), pp. 555–561. doi: [10.1148/radiology.192.2.8029431](https://doi.org/10.1148/radiology.192.2.8029431).
- [37] H. Yu, A. Shimakawa, C. A. McKenzie, E. Brodsky, J. H. Brittain, and S. B. Reeder. “Multiecho water-fat separation and simultaneous R_2^* estimation with multifrequency fat spectrum modeling.” In: *Magnetic Resonance in Medicine* 60.5 (Nov. 2008), pp. 1122–1134. doi: [10.1002/mrm.21737](https://doi.org/10.1002/mrm.21737).
- [38] Liang Zhi-Pei. “A model-based method for phase unwrapping.” In: *IEEE Transactions on Medical Imaging* 15.6 (1996), pp. 893–897. ISSN: 0278-0062.

APPENDIX

APPENDIX

A.1 TESTING DIFFERENT MODELING FUNCTIONS FOR B_1

The results presented in the modeling of the B_1 phase contributions make use of the second degree 3D polynomial. This choice may seem only convenient at first, but to keep the body of the thesis short, the test with other initialization functions are briefly analyzed here, in the appendix section.

2^{nd} versus 4^{th} degree 3D polynomial

Since the B_1 shape has a distinctive curvature that resembles an upward bowl, it leads to the notion that even-degree 3D polynomials are a good fit for modeling these phase contributions. Hence, we decided to test the water-fat separation when a 2^{nd} and a 4^{th} degree 3D polynomial is used.

The results are presented in [Figure A.1](#). From top to bottom the red boxes indicate the important points for the comparison of both images:

- **Cervical Spine:** The brain separation is slightly superior for the second degree polynomial, since for low and medium regularization the fat content of the brain is depicted higher for the fourth degree polynomial. It can also be noted how for high regularization the fat of the bone is depicted better in the second degree polynomial.
- **Thoracic Spine:** At high regularization it appears that the second degree polynomial is more stable by its bone separation into fat and water.
- **Lumbar Spine:** Once again, at high regularization the separation seems more robust for fat and water in the second degree polynomial.

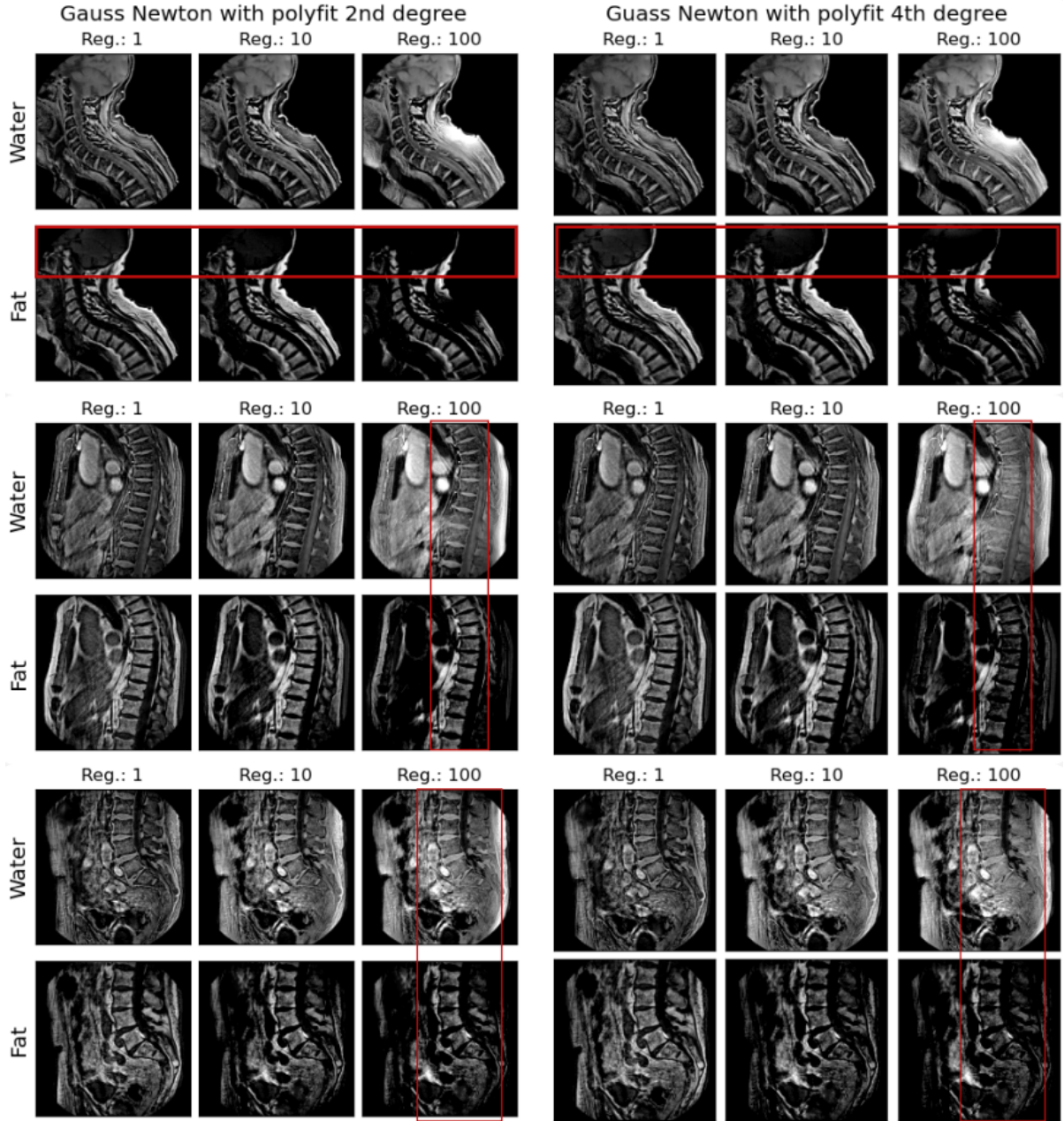


Figure A.1: Water-Fat separation comparison of the fitting functions 2^{nd} versus 4^{th} degree 3D polynomial for initialization. From top to bottom the cervical spine, thoracic spine and lumbar spine results are depicted. The red boxes indicate the important points for the comparison of both images. The second degree polynomial seems the superior choice between the two.

Since for the cervical spine the differences are subtle, the line-plots through the brain of both ϕ^* are compared. The resulting image is given in [Figure A.2](#). The 4^{th} degree polynomial over-fits the anatomy slightly as seen from the

line-plots, whereas using the plain 2^{nd} degree polynomial acts as an implicit regularizer, since the starting point is much more robust.

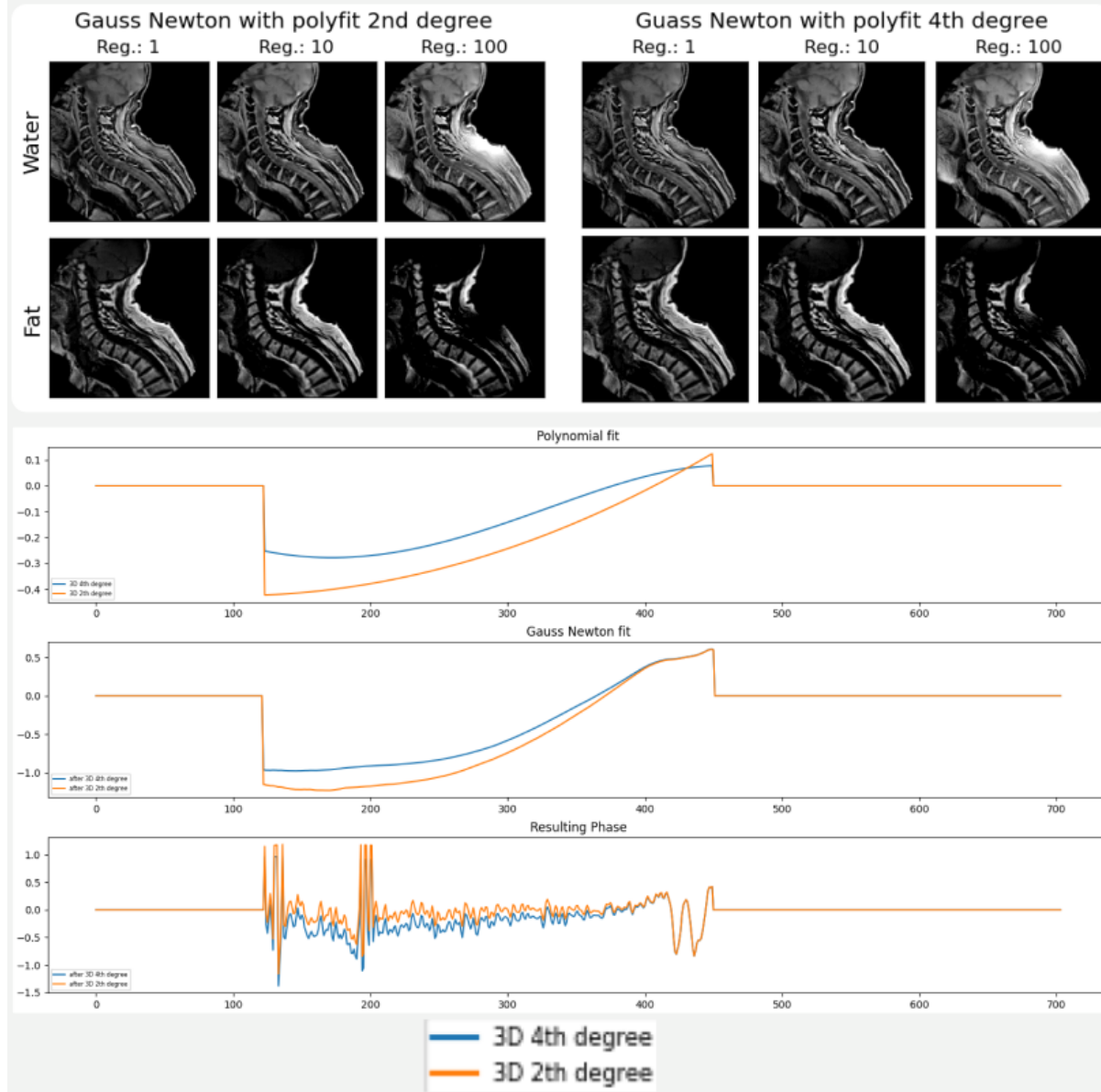


Figure A.2: Water-Fat separation and line-plot comparison of the fitting functions 2^{nd} versus 4^{th} degree 3D polynomial for initialization. It is illustrated how the 4^{th} degree polynomial over-fits the image slightly, whereas, the 2^{nd} degree polynomial acts an implicit regularizer because of its coarseness.

2^{nd} degree 3D polynomial vs plain UTE phase initialization

Another line of reasoning lead to the idea that if the first ϕ is initialized as the UTE phase of the raw scan the iterative optimization algorithm will reduce its effort on *fitting* the image and more on *smoothing* it. Thus, having a better fit.

The results are depicted in [Figure A.3](#). From top to bottom we discuss:

- **Cervical Spine:** The brain separation is better in the second degree polynomial than in the UTE phase initialized result, since the fat content of the brain in the latter is higher as highlighted by the **red** box. However, the stability at the edges seem to be better for the UTE phase initialized method, as seen in the **blue** box.
- **Thoracic Spine:** The water-fat separation for high regularization is clearly better in the case of the 2^{nd} degree polynomial, since the water content of bone in the UTE phase initialized method is slightly higher than expected.
- **Lumbar Spine:** For mid and high regularization the water-fat separation from the second degree polynomial delivers better results than the UTE phase initialized method. Specifically, the bone is correctly depicted in the former, whereas it lacks stability in the latter.

Conclusion

Having showed that the 2^{nd} degree 3D polynomial is superior for both cases, the choice is made to continue the study analysis using this polynomial function for fitting B_1 and use the fit to initialize ϕ, W, F .

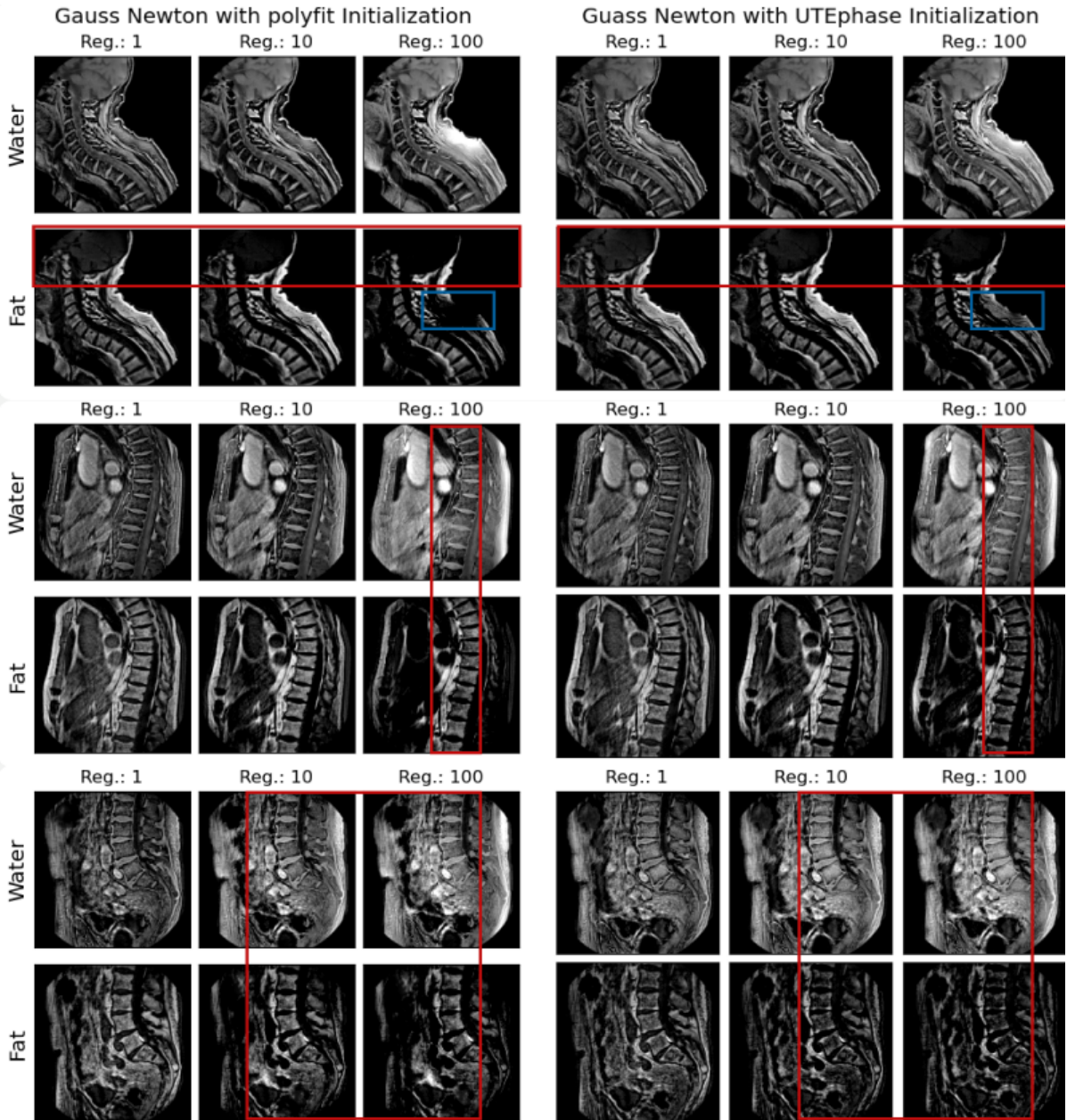


Figure A.3: Water-Fat separation comparison of the fitting functions 2nd degree 3D polynomial versus using the UTE phase for initialization. From top to bottom the cervical spine, thoracic spine and lumbar spine results are depicted. The red and blue boxes indicate the important points for the comparison of both images. The second degree polynomial seems the superior choice between the two. Although in the cervical spine the UTE phase initialization reduces the anatomy edges artifacts.

A.2 ADDITIONAL CLINICAL ANATOMIES

For the effects of initialization on water-fat separation in [Section 7.2](#). Only the cervical, thoracic and lumbar spine are depicted. However, other anatomies are also analyzed briefly in the appendix for completeness.

First, the water-fat separation of a knee is depicted in [Figure A.4](#). The results are uninteresting since initialization seems to not have a noticeable impact on the water-fat separation of the anatomy.

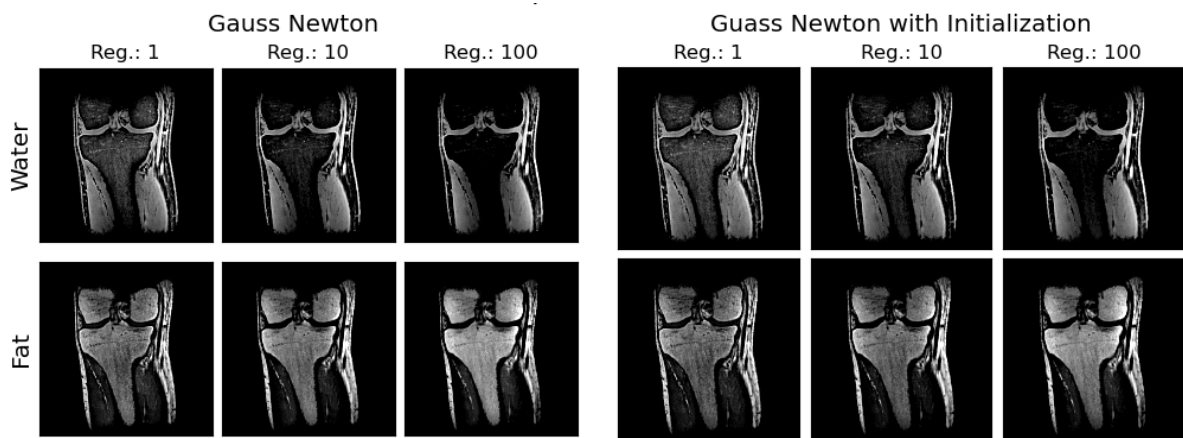


Figure A.4: Water-Fat separation of the Knee for the plain Gauss Newton and the initialized method. There is no visible difference between both methods.

Second, a coronal thoracic scan is analyzed.

In [Figure A.5](#) the lung water-fat separation is shown. The initialization affects positively the separation for low and high regularization, shifting the heart to water, as expected, for $\lambda = 1$, and increasing stability for high regularization. For $\lambda = 10$ the results are very similar.

From the same scan a slice of the liver is depicted in [Figure A.6](#). This region is specially difficult since the effect of the air-filled lung alters the phase at the transition regions between different tissues. The initialized method correctly shifts the liver region to water for all λ s, but not completely, having a partially correct separation. However, better than the non-initialized method.

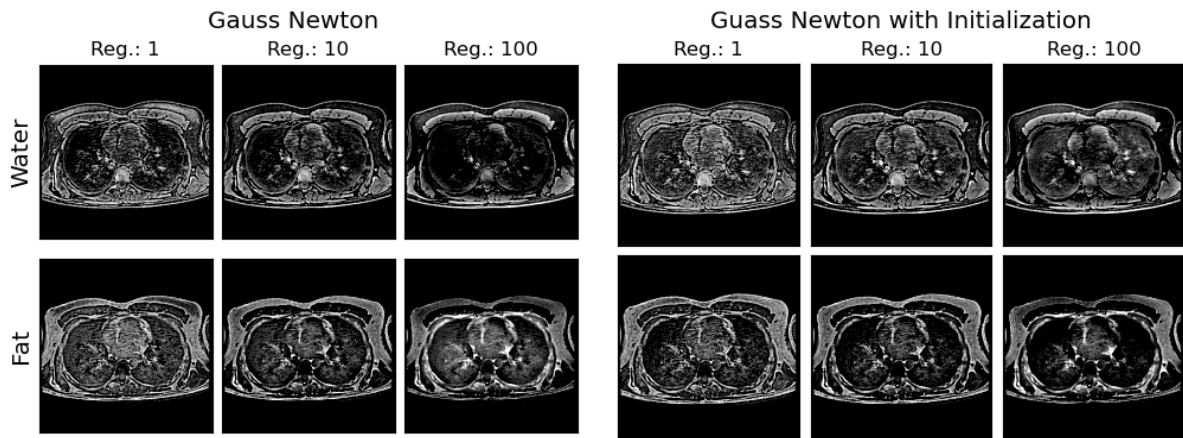


Figure A.5: Water-Fat separation of the Lung for the plain Gauss Newton and the initialized method. There is improvement of the water-fat separation at low regularization, since the heart has more content of water in the initialized method. For high regularization, the initialized method depicts the separation better and its more stable. Mid regularization results show no discernible difference.

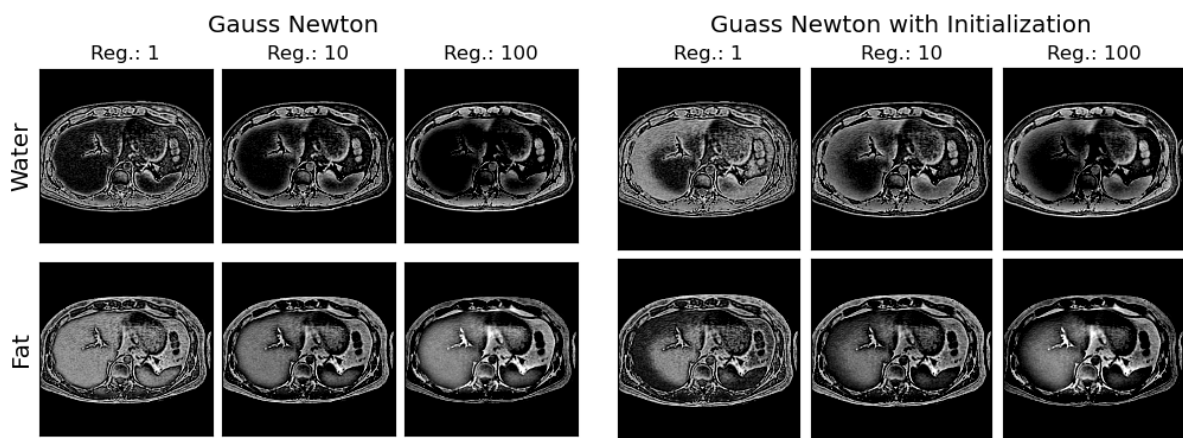


Figure A.6: Water-Fat separation of the liver for the plain Gauss Newton and the initialized method. The initialized method partially reassigned the liver region to water across all λ values, resulting in a separation that, while not entirely accurate, is substantially more correct than that achieved by the non-initialized method.